





Article

Performance Enhancement of Direct Torque and Rotor Flux Control (DTRFC) of a Three-Phase Induction Motor Over the Entire Speed Range: Experimental Validation[†]

Mussaab M. Alshbib ¹, Mohamed Mussa Elgbaily ^{2,*}, Ibrahim Mohd Alsofyani ³ and Fatih Anayi ²

¹ Mechatronics and Laboratory Engineering Department, Sham University, Aleppo 11566, Syria

² Wolfson Centre for Magnetics, School of Engineering, Cardiff University, Cardiff CF24 3AA, UK

³ Department of Electrical and Computer Engineering, Ajou University, World cup-ro 206, Yeongtong-gu, Suwon 16499, Republic of Korea

* Correspondence: elgbailymm@cardiff.ac.uk; Tel.: +44-7405019533

[†] This paper is an extended version of our paper published in the 1st International Electronic Conference on Machines and Applications (IECMA 2022).

Abstract: This paper proposes a robust and effective method of direct torque and rotor flux control (DTRFC) strategy for an induction motor (IM). The described scheme ensures the elimination of uncontrollable angles (UCAs) over the entire speed range. This means that each voltage vector (VV) produces the required effect of both torque and flux without any counteracting effect. First, the behaviour of the DTRFC algorithm was analysed at low and high speeds in terms of determining the values of UCAs. Through the analysis, it was found that the basic scheme suffered from UCAs at medium and high speeds. Accordingly, a special strategy for medium and high speeds with 18 sub-sectors (SSs) was proposed while maintaining the basic 6 sectors strategy for low speed. The transition speed between the two strategies was determined to ensure the absence of UCAs over the whole speed range. The simulation results of the proposed method were obtained in the MATLAB/Simulink environment. Furthermore, to verify the effectiveness of this method, a dSPACE-based experimental induction motor DTRFC drive system was accomplished.

Keywords: adjustable speed drives; direct torque and rotor flux control (DTRFC); voltage source inverter; Lookup table



Citation: Alshbib, M.M.; Elgbaily, M.M.; Alsofyani I.M.; Anayi F. Performance Enhancement of Direct Torque and Rotor Flux Control (DTRFC) of a Three-Phase Induction Motor Over the Entire Speed Range: Experimental Validation. *Machines* **2023**, *11*, 22. <https://doi.org/10.3390/machines11010022>

Academic Editor: Antonio J. Marques Cardoso, Dan Zhang, Giuseppe Carbone

Received: 24 October 2022
Revised: 17 December 2022
Accepted: 19 December 2022
Published: 25 December 2022



Copyright: © 2022 by the authors. Licensee MDPI, Basel, Switzerland. This article is an open access article distributed under the terms and conditions of the Creative Commons Attribution (CC BY) license (<https://creativecommons.org/licenses/by/4.0/>).

1. Introduction

In variable AC control systems, the inverter (VSI) is used to drive the AC motors as variable-frequency voltage or current sources. One of the various methods used for controlling the machine's torque and speed is Direct Torque Control (DTC) [1,2]. The DTC is known for its fast response algorithm, ease of structure, and strong robustness in the face of parameter uncertainties and perturbations [3]. The configuration is much simpler than the Field Oriented Control (FOC) system due to the absence of a frame transformer, a pulse width stage, and a position sensor [4]. Several modifications and improvements have been made to the original control structure in order to overcome the problems associated with the DTC drive, namely the high electromagnetic torque ripple and the variable switching frequency [5]. In reference [6], an analysis of the VVs' effects on the state variables (torque and rotor flux) over the sector and speed ranges based on the DTRFC algorithm was introduced, which uses the rotor flux as a controlled variable instead of the stator flux used in the traditional DTC algorithm because DTRFC is able to operate with torque ranges that exceed the nominal torque as far as the dc-link of the inverter allows. These showed that some abnormality states called uncontrollable angles (UCAs) exist in which it is not possible to guarantee the correct control of the flux and torque. Reference [7] proposed a sequence of three VVs at a constant sample period in order to reduce the ripples of the torque and the

rotor flux. A Unified Flux Control (UFC) algorithm was suggested in [8] to reduce the flux and the torque ripples over a fixed sampling time. A minimum distance vector selection scheme replaced the switching vector Lookup Table (LUT) for the least unified flux error. To reduce the flux and torque errors, an approach was introduced by inserting the zero VV along with the selected VV [9,10], while the zero-voltage vector was eliminated, resulting in a fast torque response in the transient state [11]. A sequential strategy integrated with the duty ratio optimisation algorithm was proposed in [12] to select the optimal voltage vector which can significantly alleviate the torque ripple. To increase the torque loop bandwidth, a frequency carrier was proposed for the constant frequency torque controller-based DTC (CFTC-DTC) of the IM [13]. The proposed carrier reduced the effect of the ohmic drop when long zero-voltage vectors were selected. The application of odd or even VVs in the sectors allowed reducing the common-mode emissions [14,15]. However, this attempt was made at the expense of an increase in the torque, the flux ripples, and the harmonic content of the voltage and current waveforms. The reference [16] proposed a DTC controller that integrates feedback linearisation (FBL) together with sliding mode control (SMC). The main advantage of the FBL over the classical DTC is that the results of the linear control theory can be easily applied to obtain a better performance. Similarly, the Fuzzy-2 Direct Torque Control algorithm (F2DTC) was proposed by Naik in [17]. A sensorless DTC scheme was implemented in [18] for a two-level voltage source inverter (VSI)-fed IM drive where the constant switching frequency controller (CSFC) is used for flux regulation. However, it affects the torque response and the PI regulator needs to be tuned well. As for low speed, DTC fails due to poor flux regulation. Therefore, two dynamic hysteresis torque band (DHTB) strategies for the conventional DTC were proposed to solve this problem [19] by dynamically altering the amplitude of the hysteresis torque band based on a flux error range. In [20], a composite torque-regulator-based DTC scheme was proposed for torque tracking optimisation in PMSM drives. A universal LUT-based DTC is proposed for OW-PMSM drives under different conditions of the dc-link voltage ratio [21]. The distribution criterion of VVs under various dc-link voltage ratios was analysed, and the VVs were assigned to different regions by designing a generalised region division scheme. A DTC method based on minimum voltage vector (VV) error was proposed in [22]. The proposed strategy effectively optimised the duty ratio of fundamental VV to minimise the error between the reference VV and the final VV imposed on motor terminals. A duty-ratio controller that considers the operating speed effect on the change of torque was proposed in [23]. It avoids using the voltage vectors that produce high torque ripples, therefore reducing the noise of the motor. The new approach of the Genetic Algorithm (GA) and Particle Swarm Optimisation (PSO)-based DTC was proposed in [24] to obtain low torque ripples and improve the driving system's efficiency. Recently, many studies in the field of the DTC algorithm increase the number of sectors within the DTC scheme, which are: 12 sub-sectors [25–28], 18 sub-sectors [29–31], or 24 sub-sectors [32]. In the last aforementioned articles, with different numbers of sectors, the main objective of each is to reduce the ripples of torque and magnetic flux. Moreover, the switching table that was placed in each of them was not the result of an analytical study but rather an experience by the researcher. The authors of [33] presented the indirect torque control of PMSM with two loops based on PI controllers and MPC. The MPC loop served to reduce the computational burden on the system. The system was then developed in [34] by incorporating a deep neural network (DNN) with MPC, which added four quadrants of the operation range. MPC was also employed to enhance the efficiency of the nonlinear PMSM model in [35] via the voltage component vector in space vector modulation. However, MPC was utilised in [36] in order to reduce the torque chattering and minimise IM drive system losses. However, experimental validation was not accomplished. Hybrid MPC and fuzzy logic approaches were implemented in electric vehicles in [37] to ensure the control of the PMSM and energy management system.

Consequently, there was a lack of knowledge regarding the actual effect of each VV on the flux and torque within the whole sector range. After analysing the existing literature on

the topic of UCAs, This study recognised the limitations of the researches that addressed this issue, and was only conducted in the context of the overall field of speed.

This article suggests an enhanced DTRFC strategy that aims to eliminate the UCAs over a wide speed range. The proposed method uses 18 SSs to overcome the issues of conventional 6 SSs DTRFC at medium and high speeds in terms of the UCAs. In addition, a universal scheme could be synthesised to allow applying the inverter pulses from 6 SSs DTRFC or from 18-SSs DTRFC according to the transition speed at which the UCAs begin to appear. Simulations and experimental results are presented to show and compare the effectiveness of the proposed 18 SSs scheme in the DTRFC algorithm of the induction motor.

2. Theories and Principles

The instantaneous control of rotor flux modulus and electromagnetic torque summarises the fundamental principle of the direct torque and rotor flux algorithm. Both are governed by intermediate control loops with no current control loops. Generally, the error signals of the rotor flux and electromagnetic torque are obtained by comparing the reference signals to the estimated signals. To complete the control process, error signals are introduced into two independent hysteresis regulators. [31]. The general block diagram of the conventional DTRFC algorithm can be constructed as shown in Figure 1.

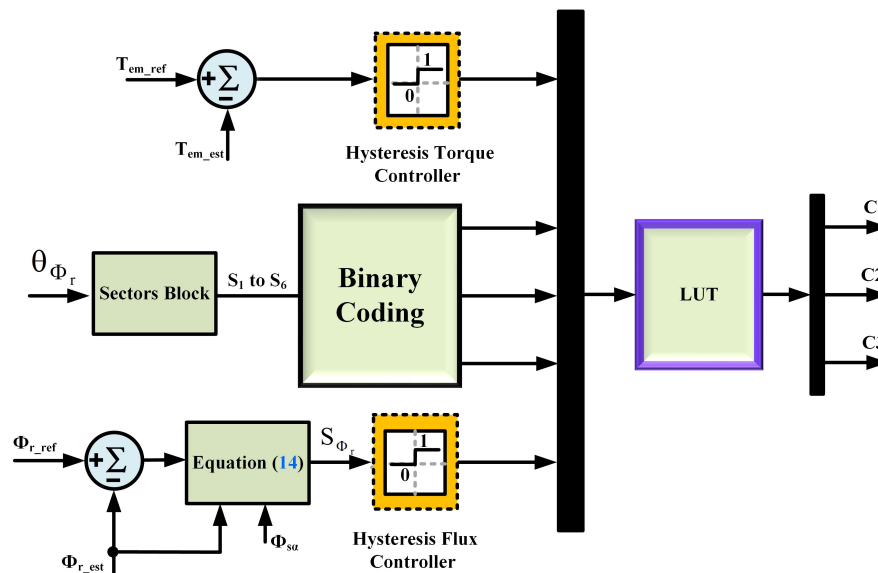


Figure 1. The block diagram of DTRFC scheme.

The four active vectors to control both the stator flux and the electromagnetic torque in DTC algorithm are shown in Table 1 [6].

Table 1. Conventional switching table in DTC algorithm.

S_{Tem}	S_{Φ_r}	6-Sector Index					
		1	2	3	4	5	6
0	0	V ₅	V ₆	V ₁	V ₂	V ₃	V ₄
	1	V ₆	V ₁	V ₂	V ₃	V ₄	V ₅
1	0	V ₃	V ₄	V ₅	V ₆	V ₁	V ₂
	1	V ₂	V ₃	V ₄	V ₅	V ₆	V ₁

The two components of the rotor flux vector are estimated in the stator reference frame ($\alpha^s - \beta^s$) as in (1) and (2) [32].

$$\Phi_{ra}^s = \frac{L_r}{L_m} (\Phi_{sa}^s - \sigma L_s i_{sa}^s) \tag{1}$$

$$\Phi_{r\beta}^s = \frac{L_r}{L_m} \left(\Phi_{s\beta}^s - \sigma L_s i_{s\beta}^s \right) \quad (2)$$

where L_m is the mutual inductance; L_s and L_r are the stator and the rotor self inductances, respectively; $i_{s\alpha}^s$ and $i_{s\beta}^s$ are vector components of stator current. $\Phi_{s\alpha}^s$ and $\Phi_{s\beta}^s$ are vector components of stator flux; σ is leakage factor = $1 - \frac{L_m^2}{L_s L_r}$. The position of the rotor flux vector is estimated in the stationary reference frame, $(\alpha^s - \beta^s)$ as in (3) [6].

$$\theta_{\Phi_r} = \arctan \left(\frac{\Phi_{r\beta}^s}{\Phi_{r\alpha}^s} \right) \quad (3)$$

The two components of the voltage vector produced by the inverter are calculated in the synchronous reference frame, $(\alpha - \beta)$, as in (4) and (5).

$$V_{s\alpha} = \sqrt{\frac{2}{3}} E \cos \left(\frac{k-1}{3} \pi - \theta_{\Phi_r} \right) \quad (4)$$

$$V_{s\beta} = \sqrt{\frac{2}{3}} E \sin \left(\frac{k-1}{3} \pi - \theta_{\Phi_r} \right) \quad (5)$$

where k is the sector index ($k = 1, 2, \dots, 6$); E is the DC-link voltage. For the sake of simplicity, the rotor flux vector is oriented according to α -coordinate axis. Thus, the imaginary component of the rotor flux vector becomes zero, i.e., in (6).

$$\Phi_{r\beta} = 0 \quad , \quad \Phi_r = \Phi_r = \Phi_{r\alpha} \quad (6)$$

Orienting the rotor flux vector in the direction of the α -coordinate axis, the rotor flux modulus, the slip frequency, and the synchronous speed can be found in the synchronous reference frame, $(\alpha - \beta)$ in (7)–(9), [38].

$$\Phi_r = \frac{L_m}{L_s} \Phi_{s\alpha} = L_m i_{s\alpha} \quad (7)$$

$$\omega_r = \frac{L_m}{\sigma L_s \tau_r} \frac{\Phi_{s\beta}}{\Phi_r} = \frac{L_m}{\tau_r} \frac{i_{s\beta}}{\Phi_r} \quad (8)$$

$$\omega_s = \omega + \omega_r \quad (9)$$

where τ_r is the rotor time constant; ω is the rotor speed; and ω_r is the slip frequency.

The two components of the stator current in the synchronous reference frame can be obtained from the two components in the stationary reference frame in (10) and (11), [39,40].

$$i_{s\alpha} = i_{s\alpha}^s \cos \theta_s + i_{s\beta}^s \sin \theta_s \quad (10)$$

$$i_{s\beta} = -i_{s\alpha}^s \sin \theta_s + i_{s\beta}^s \cos \theta_s \quad (11)$$

where θ_s is the orientation angle and is equal to $\theta_s = \int \omega_s \cdot dt$.

In the same frame, the electromagnetic torque can be expressed in (12) [41].

$$T_{em} = \frac{p L_m}{\sigma L_s L_r} (\Phi_{r\alpha} \Phi_{s\beta} - \Phi_{r\beta} \Phi_{s\alpha}) = \frac{p L_m}{\sigma L_s L_r} (\Phi_{r\alpha} \Phi_{s\beta}) \quad (12)$$

By using the Equations (8), the Equation (12) can be rewritten in (13).

$$T_{em} = \frac{p L_m}{L_r} (\Phi_r i_{s\beta}) \quad (13)$$

To complete the analytical study of the DTRFC algorithm, it is necessary to have the equations of the flux and torque errors and their derivatives in (14)–(17) [6].

$$S_{\Phi_r} = k_{\Phi_r}(\Phi_{r-ref} - \Phi_r) \left(\frac{L_m}{\sigma L_s \tau_r} \operatorname{Re}(\underline{\Phi}_s) - \left(\frac{1}{\sigma \tau_r} \right) \Phi_r \right) \quad (14)$$

$$\frac{dS_{\Phi_r}}{dt} = -\frac{d\Phi_r}{dt} \left(k_{\Phi_r} - \frac{1}{\sigma \tau_r} \right) - \frac{L_m}{\sigma L_s \tau_r} [\operatorname{Re}(\underline{V}_s - R_s i_s - j\omega_s \underline{\Phi}_s)] \quad (15)$$

$$S_{T_{em}} = T_{em-ref} - T_{em-est} \quad (16)$$

$$\frac{dS_{T_{em}}}{dt} = -\frac{dT_{em-est}}{dt} = \left(\frac{1}{\sigma \tau_s} + \frac{1}{\sigma \tau_r} \right) T_{em} - \frac{pL_m}{\sigma L_s L_r} \operatorname{Im}[\underline{V}_s \underline{\Phi}_r^* - j\omega \underline{\Phi}_s \underline{\Phi}_r^*] \quad (17)$$

where k_{Φ_r} is an optional positive constant; \underline{V}_s is a rotary voltage vector representing one of the six vectors which are produced by the VSI driving the induction motor.

3. The Effect of VVs at Low Speeds in the DTRFC Algorithm

Figure 2 shows that the UCAs do not appear at low speeds when controlling the torque. On the contrary, two UCAs appear when controlling the rotor flux resulting from the two vectors $\underline{V}_{i+1}, \underline{V}_{i-1}$. To analyse the performance of the DTRFC algorithm at low speed ($20\% \omega_n$). Equations (15) and (17) are used for the nominal load value.

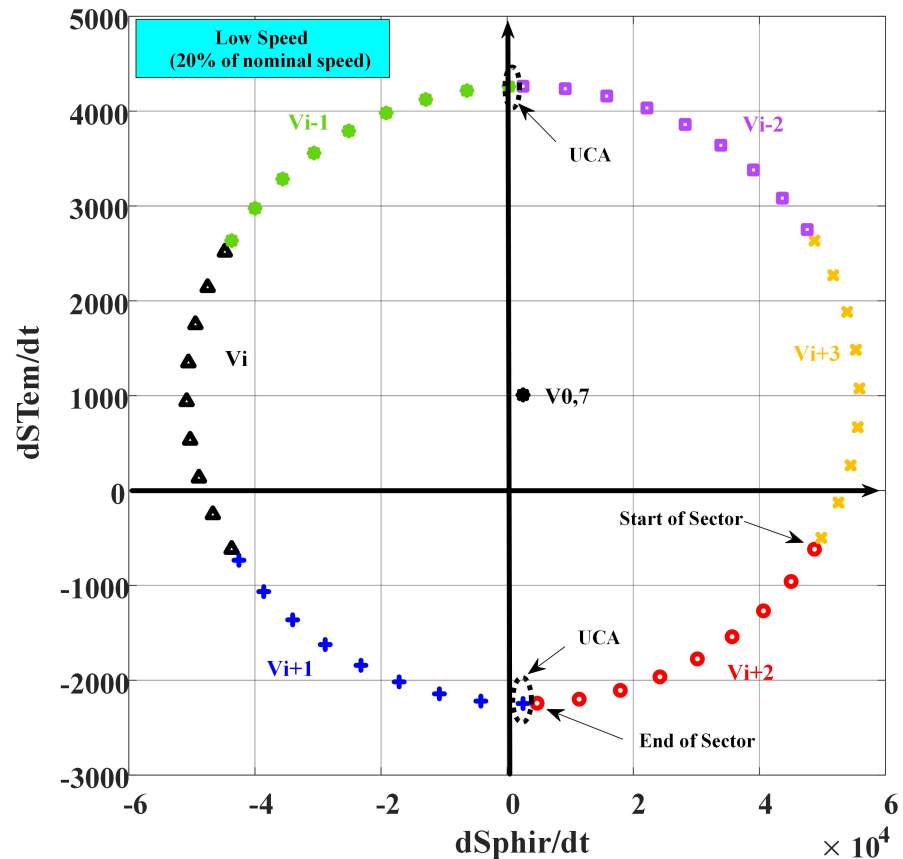


Figure 2. Values of dS_{Φ_r} and $dS_{T_{em}}$ for low positive speed ($20\% \omega_n$).

Furthermore, in Figure 2 shows the values of the two functions dS_{Φ_r} and $dS_{T_{em}}$, while the rotor flux vector scans the entire sector for positive speed and nominal load. One can easily notice that the four active vectors $\underline{V}_{i+1}, \underline{V}_{i+2}, \underline{V}_{i-1}$, and \underline{V}_{i-2} produce the same sign of dT_{em} over the entire sector. Conversely, this is not maintained for function dS_{Φ_r} . For

greater clarification, the function dS_{Φ_r} does not sustain the same positive sign during the application of the two voltage vectors, \underline{V}_{i+1} at the beginning of the sector, \underline{V}_{i-1} at the end of the sector.

4. The Effect of VVs at High Speeds in DTRFC Algorithm

The error derivations of the rotor flux and torque, dS_{Φ_r} and $dS_{T_{em}}$ are plotted at high positive speed, ($75\% \omega_n$) as shown Figure 3 during the rotor flux vector movement over the sector. It is noted according to the sign of the two mentioned functions that it is not maintained over the entire sector, as there are some effective VVs showing an opposite effect to what was expected. For instance, the vector \underline{V}_{i-2} shows a negative change of dS_{Φ_r} at the end of the sector, on the contrary to what is expected (i.e., there is UCA). On the other hand, the two vectors $\underline{V}_{i+2}, \underline{V}_{i+1}$ cause a positive change of $dS_{T_{em}}$ at the beginning and the end of the sector, respectively, on the contrary to what is expected (i.e., there are UCAs).

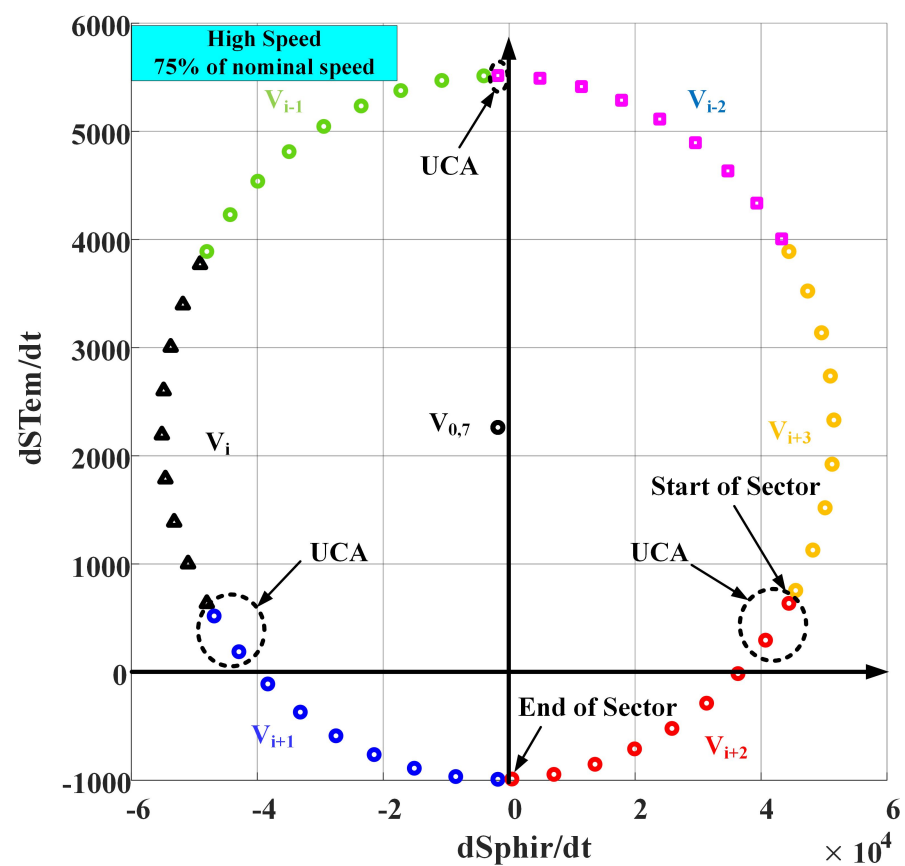


Figure 3. Values of dS_{Φ_r} and $dS_{T_{em}}$ for positive high speed ($75\% \omega_n$).

5. Determination of UCAs Values at Low and High Speeds

Figure 4 shows the effect of applying the two vectors \underline{V}_{i+1} and \underline{V}_{i-1} on the function dS_{Φ_r} at low speed ($20\% \omega_n$). It can be observed that there are two uncontrollable angles at the beginning and the end of the sector. Each of them has a value equal to 2.5° (4% of the sector range).

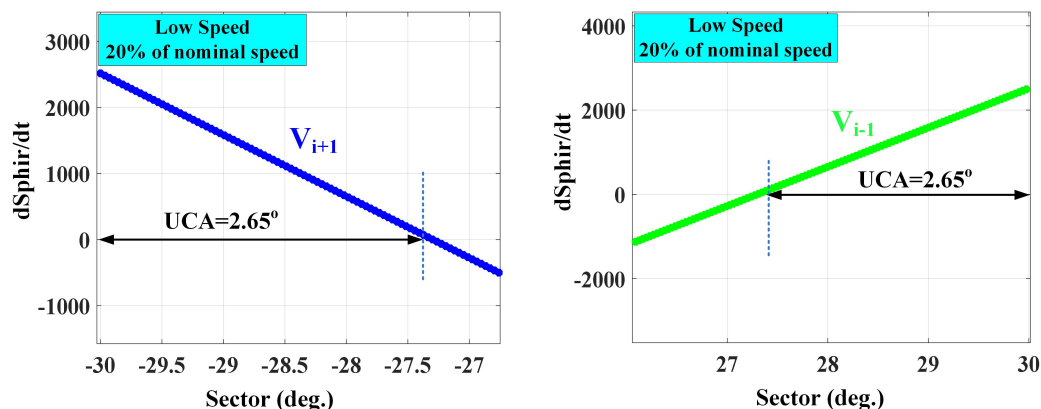


Figure 4. UCA of V_{i+1} or V_{i-1} on dS_{Φ_r} for low speed ($20\% \omega_n$).

Figure 5 shows the effect of applying the two vectors V_{i+2}, V_{i-2} on the function dS_{Φ_r} at high speed ($75\% \omega_n$). It can be observed that there are two uncontrollable angles at the beginning and the end of the sector. The two values are 1.86° (3% of the sector range). It can be concluded that the change of speed from low to high has a slight effect on the uncontrollable angles of the function dS_{Φ_r} .

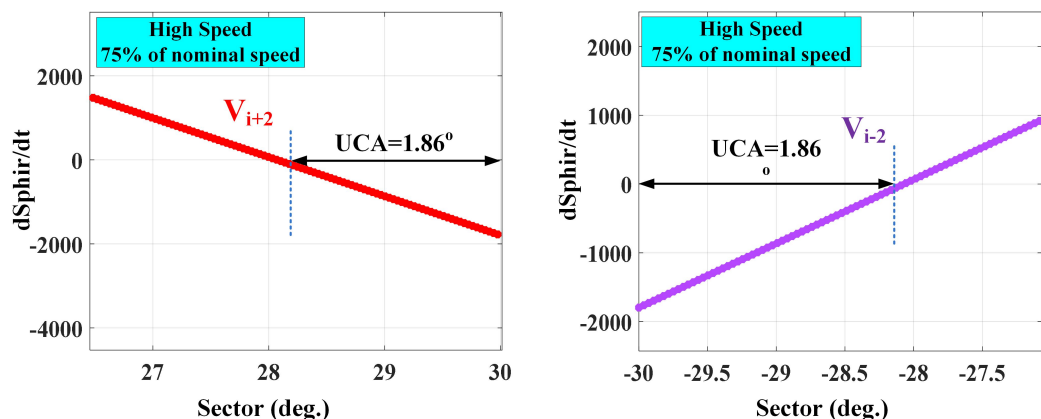


Figure 5. UCA of V_{i+2} or V_{i-2} on dS_{Φ_r} for high speed ($75\% \omega_n$).

Figure 6 shows the UCA of the two vectors V_{i+1}, V_{i+2} for the function dS_{Tem} at high speed ($75\% \omega_n$). It can be observed that there are two UCAs at the beginning and the end of the sector. Each of them has a value equal to 13.5° (22% of the sector range).

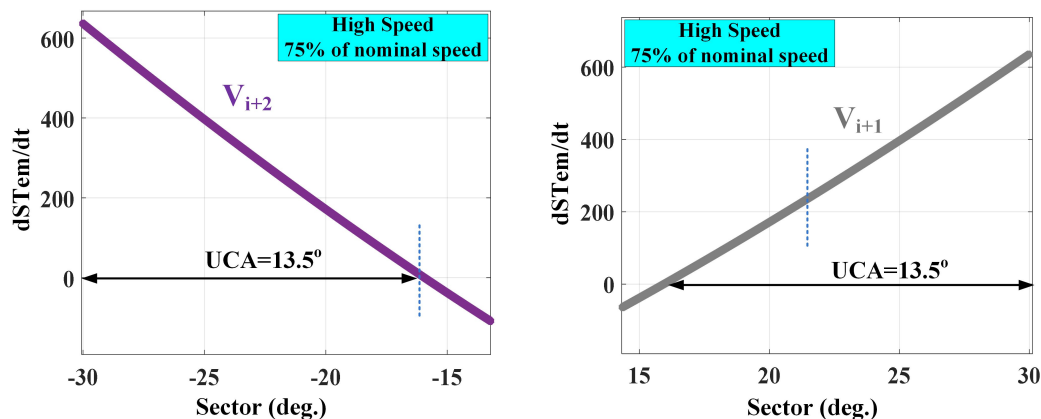


Figure 6. UCA of V_{i+2} or V_{i+1} on dS_{Tem} for high speed ($75\% \omega_n$).

It is noted that the effect of the UCAs on the function dT_{em} at the beginning and end of the sector is greater than its counterpart for dS_{Φ_r} . Priority will be given to cancelling the UCAs of dT_{em} while devising the proposed strategy, since that the UCAs of dS_{Φ_r} are small and can be neglected.

6. The Proposed 18 SSs DTRFC Strategy for Medium High Speeds

A proposed strategy suitable for working at medium and high speeds is devised in order to eliminate the UCAs when controlling the torque. The proposed strategy is based on dividing the path of the rotor flux vector into (18) unequal sub-sectors so that the sum of all three successive sectors is (60°) considering the beginning of the first SS at the corner (0°). Every three subsequent sectors will repeat the same distance after the previous three SSs, as shown in Table 2. It is sufficient to mention the ranges of the first three SSs and the last three ones of the path of rotor flux vector, while the rest of the SSs are easily deduced from the mentioned ones, as shown in Table 2. It should be noted that the division shown in Table 2 is not the only option, but there are other solutions that the designer can devise and then select the most appropriate solution that fulfils the required control requirements. Depending on Equations (15) and (17), for the first three sectors shown in Table 2, the errors derivatives for the rotor flux and the torque can be plotted for high positive speed ($75\% \omega_n$) with a nominal load, as shown in Figure 7.

Table 2. Dividing the path of the rotor flux vector into (18) SSs.

Sub-Sectors Index		
SS ₁	SS ₂	SS ₃
$0^\circ:15^\circ$	$15^\circ:45^\circ$	$45^\circ:60^\circ$
\vdots	\vdots	\vdots
SS ₁₆	SS ₁₇	SS ₁₈
$300^\circ:315^\circ$	$315^\circ:345^\circ$	$345^\circ:360^\circ$

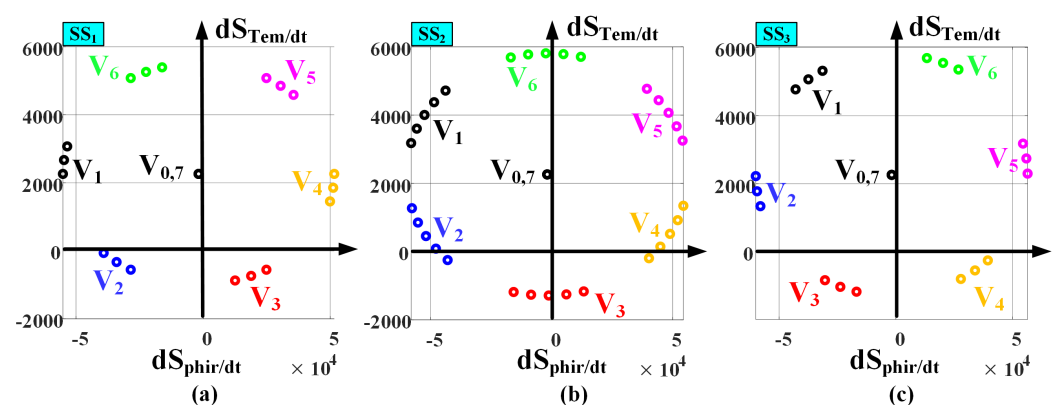


Figure 7. The errors derivatives of the rotor flux and torque for the proposed strategy at high speed ($75\% \omega_n$): (a) SS1, (b) SS2, (c) SS3.

The process for selecting the vectors that achieve the optimum case of the electromagnetic torque control (i.e., the UCAs are canceled) is carried out as follows:

- For the first sub-sector, shown in SS₁ Figure 7a, it can easily be seen that the four effective vectors (V_2, V_3, V_5, V_6) achieve the optimum condition for the two controlled functions dS_{Φ_r} and $dS_{T_{em}}$ because their sign does not reverse over the entire SS₁.
- For the second sub-sector, shown in SS₂ Figure 7b, the choice of the two vector (V_5, V_1) achieve the optimum condition of the control requirements for the two controlled functions dS_{Φ_r} and $dS_{T_{em}}$ in the first and second quadrants, respectively. However,

there is only one choice in the third and fourth quadrants, which is the vector (V_3). The latter vector fulfils the optimum control requirements for the torque without achieving that for the rotor flux as it causes UCA.

- For the third sub-sector, shown in SS_3 Figure 7c, it can easily be seen that the four effective VVs (V_3, V_4, V_6, V_1) achieve the optimum condition for the two controlled functions dS_{Φ_r} and $dS_{T_{em}}$ as long as they maintain their sign over the entire SS_3 .

Based on the above discussion, the LUT for the proposed strategy can be constructed as shown in Table 3. It is worth mentioning that, for the rest of the sub-sectors, the applied VVs are determined by increasing (1) to each VV index when moving from a sub-sector to another according to the sequence:

1. $SS_1, SS_4, SS_7, SS_{10}, SS_{13}, SS_{16}$.
2. $SS_2, SS_5, SS_8, SS_{11}, SS_{14}, SS_{17}$.
3. $SS_3, SS_6, SS_9, SS_{12}, SS_{15}, SS_{18}$.

Table 3. The LUT of the proposed strategy for (18) SSs.

$S_{T_{em}}$	S_{Φ_r}	Sub-Sectors Index																	
		1	2	3	4	5	6	7	8	9	10	11	12	13	14	15	16	17	18
0	0	V_5	V_5	V_6	V_6	V_6	V_1	V_1	V_1	V_2	V_2	V_2	V_3	V_3	V_3	V_4	V_4	V_4	V_5
	1	V_6	V_1	V_1	V_1	V_2	V_2	V_2	V_3	V_3	V_3	V_4	V_4	V_4	V_5	V_5	V_5	V_6	V_6
1	0	V_3	V_3	V_4	V_4	V_4	V_5	V_5	V_5	V_6	V_6	V_6	V_1	V_1	V_1	V_2	V_2	V_2	V_3
	1	V_2	V_3	V_3	V_3	V_4	V_4	V_4	V_5	V_5	V_5	V_6	V_6	V_6	V_1	V_1	V_1	V_2	V_2

In order to maintain simplicity at low speed and the elimination of UCAs at medium and high speeds, a transition will be allowed between the conventional strategy with (6) sectors expressed in Figure 1 for the low speed range, and the proposed strategy with (18) SSs (for medium and high speeds) as shown in Figure 8. These two strategies will operate in parallel so that each of them is ready to deliver the pulses to the inverter as required by the speed range.

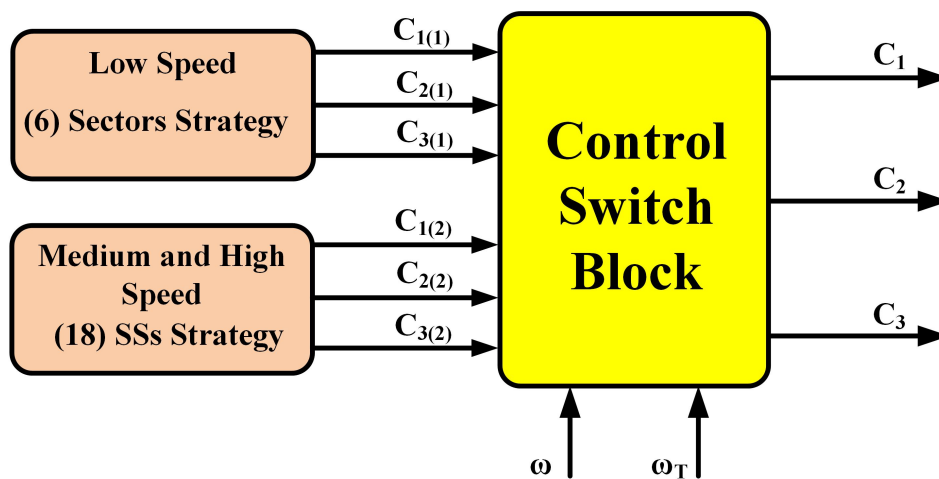


Figure 8. Block diagram of the conventional six sectors and proposed 18 SSs DTRFC strategies operating over the entire speed range.

7. Determination of the Transition Speed ω_T between the Conventional and Improved Strategy

The transitional speed ω_T is defined as the speed at which the transition from the conventional strategy (six-sector DTRFC) to the improved strategy (18-SS DTRFC) takes place [31]. This transition occurs prior to the appearance of the uncontrollable angles within the medium speed range. Thus, the careful selection of the transient speed value

ensures that the uncontrollable angles do not appear in the torque signal over the entire speed range. From this point of view, in this paragraph, the value of this speed will be determined analytically. Therefore, we return to using Equations (15) and (17). The results of the analytical study, which represent the determination of the effects of voltage vectors on each of the error variations of flux and torque, are shown in Figure 9. To clarify how the analytical result in the Figure 9 was performed, then the determination of the transition speed value, the flowchart shown in the same figure has been prepared. In fact, this flow chart represents the sequence of the analysis mentioned above to obtain the transition speed at which the UCAs starts to appear. An increment was given to the angle θ_{Φ_r} so that it scans the entire range of the sector. The speed was given a value starting from zero within an iterative loop during which the two components $v_{s\alpha}, v_{s\beta}$ were calculated according to the two equations (4 and 5). Then, the derivatives of the error function (dS_{Φ_r}, dT_{em}) were calculated according to the two Equations (15) and (17) with plotting. The process is repeated with a speed increment of (10 rad/s) given for each sector so that the calculations include all the VVs. The speed limits at which UCAs disappear were within the range of (0 : 63% ω_n) which equals (0:180 rad/s). If the speed exceeds (180 rad/s), UCAs start to appear. Thus, the value of the transition speed $\omega_T = 63\% \omega_n$ (180 rad/s) to be chosen to ensure the transition from the conventional strategy to the improved strategy.

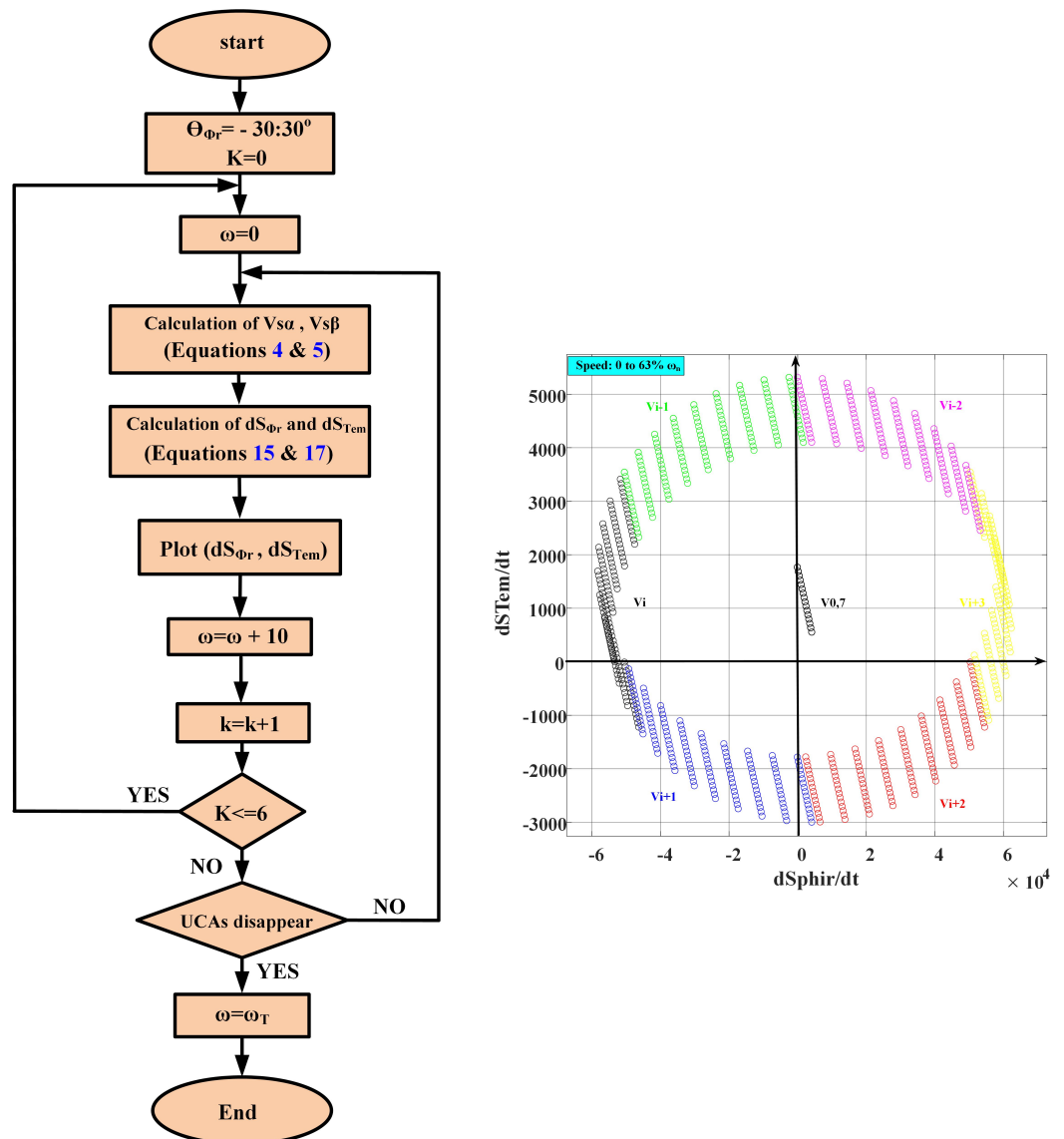


Figure 9. Change of errors of the rotor flux and torque for the range speed (0:63% ω_n).

8. Comparison of Current Case Studies toward the Proposed 18-SS DTRFC

The references [13,25,30,31,34,37] are the current studies that are among most comparable to the technique provided in this article. It should be emphasised that the cited works employ the stator flux for control, whereas the proposed technique employs the rotor flux. This indicates the possibility of producing a torque greater than the breakdown torque. In addition, the use of the classical switching table varies based on the designer’s experience in every instance, whereas the switching table in this study was determined using an analytical method that contributed to the elimination of the UCAs’ effect. Consequently, the UCAs exist in the all scenarios of the cited papers, whereas it was completely cancelled in the suggested strategy of this case study.

9. Simulation Results

The block diagram shown in Figure 8 was simulated in the MATLAB/Simulink environment for a nominal load and wide speed range with a sampling time of $T_s = 50(\mu s)$. The reference nominal values of the rotor flux and torque are: $\Phi_{r_ref} = 0.945$ (Wb), $T_{em\ ref} = 1.76$ (N.m). The two Figures 10 and 11 show the simulation results for regulating the rotor flux amplitude and the torque around their above reference values mentioned above. The controlling process of them was successful for both the conventional and the improved strategy as well as during the transition between the two strategies in the moment (3 s). The ripples amplitude of the rotor flux was 0.01 Wb for the conventional strategy, while it increased to 0.013 Wb with the improved strategy. This increase is explained by the lack of cancellation of the UCAs of the rotor flux signal in the medium- and high-speed ranges, since the priority of cancelling these angles was given to the electromagnetic torque. However, the torque ripples amplitude was 0.55 N.m for both the conventional 6-sector and improved 18-SS DTRFC strategies.

Figure 12 shows the motor speed response ω with the transition speed ω_T . The conventional strategy was worked out for a low speed value $0.28 * \omega_n$ (79 rad/s) within the time range (0:3 s), while an improved strategy worked with a speed value $0.75 * \Phi_n$ (210 rad/s) for CW and CCW. The speed of $(63% \omega_n)$, which is equal to (180 rad/s), was chosen as a transition value between the conventional (6) sector DTRFC strategy and the improved one (18 SSs). Figures 13 and 14 show the stator motor currents. The three-phase currents are sinusoidal without any ripples being noticed once the transition occurs from the conventional algorithm to the improved one. The two phase currents $i_{s\alpha}, i_{s\beta}$, according to the Equations (7) and (13), have a shape identical to both the rotor flux and torque responses, respectively [37].

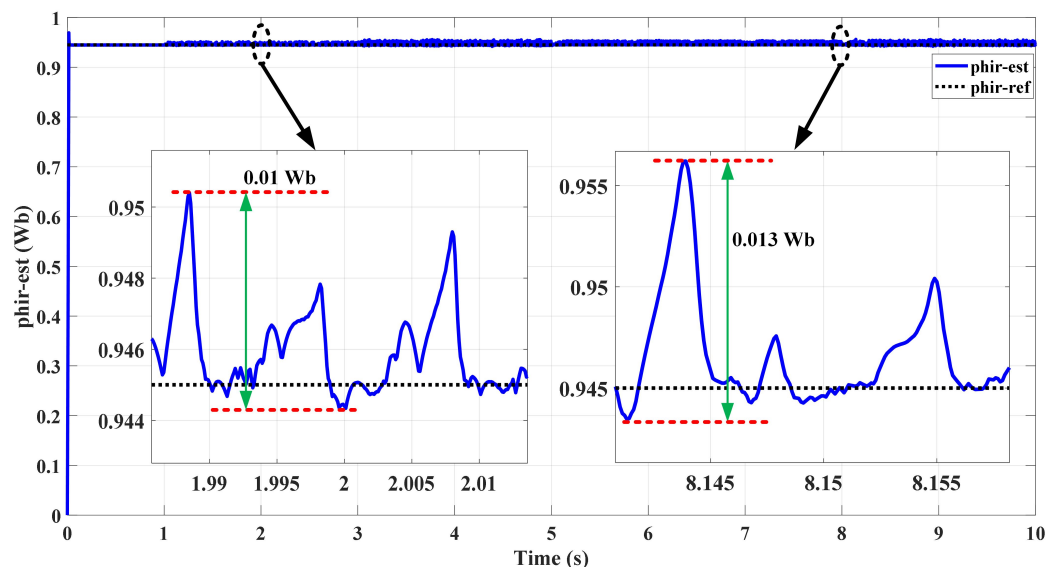


Figure 10. Rotor flux response for the conventional and the improved strategies.

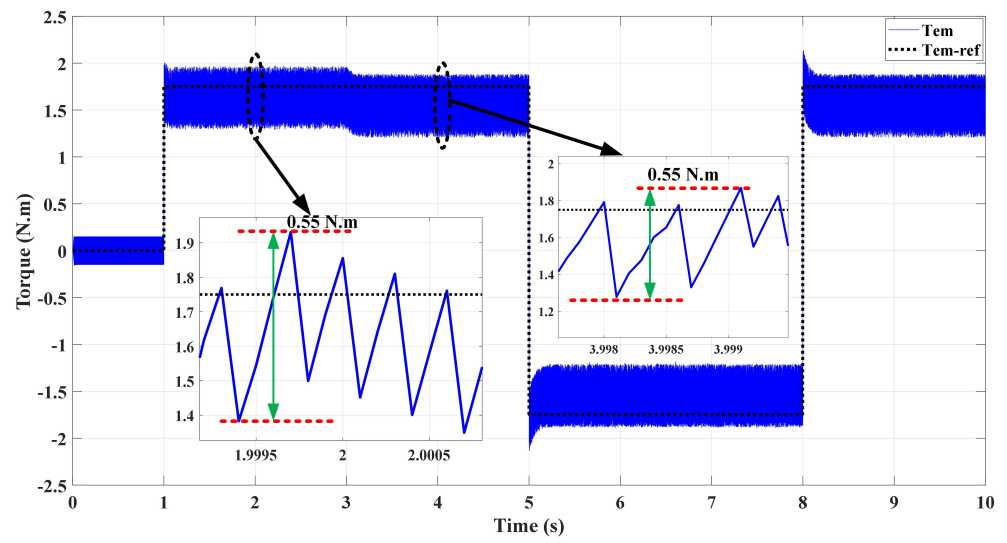


Figure 11. Torque response for the conventional and the improved strategies.

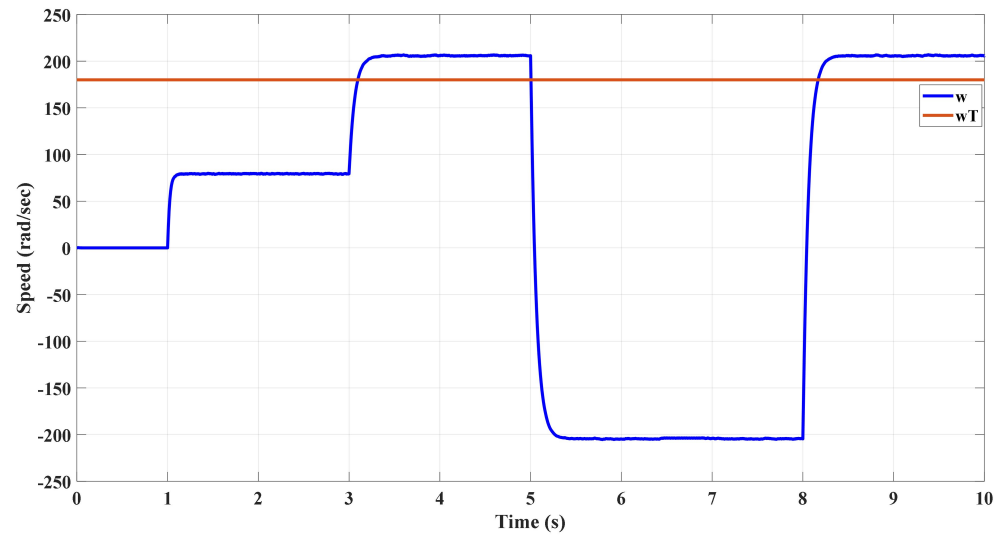


Figure 12. Motor speed and ω_T for the conventional and improved strategies.

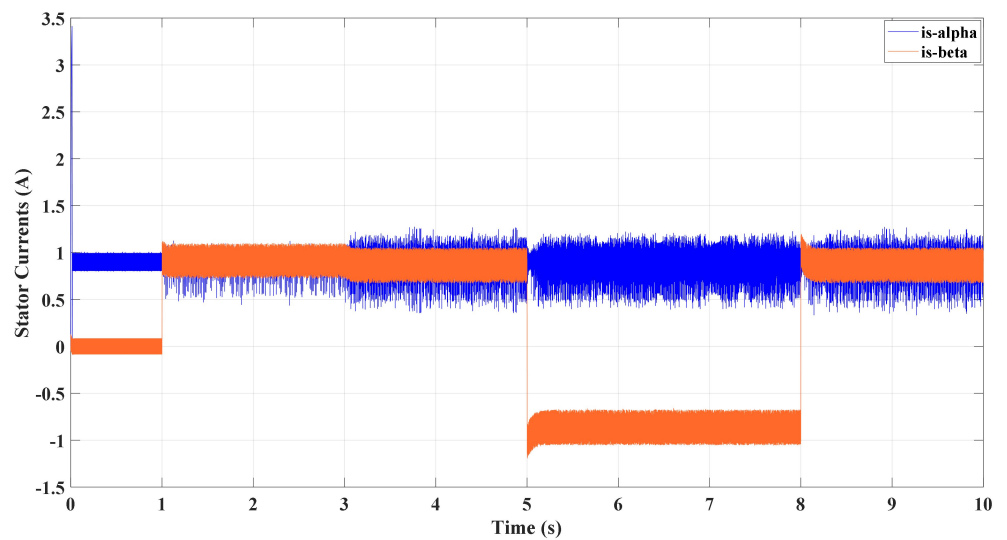


Figure 13. Two-phase currents for the conventional and improved strategies.

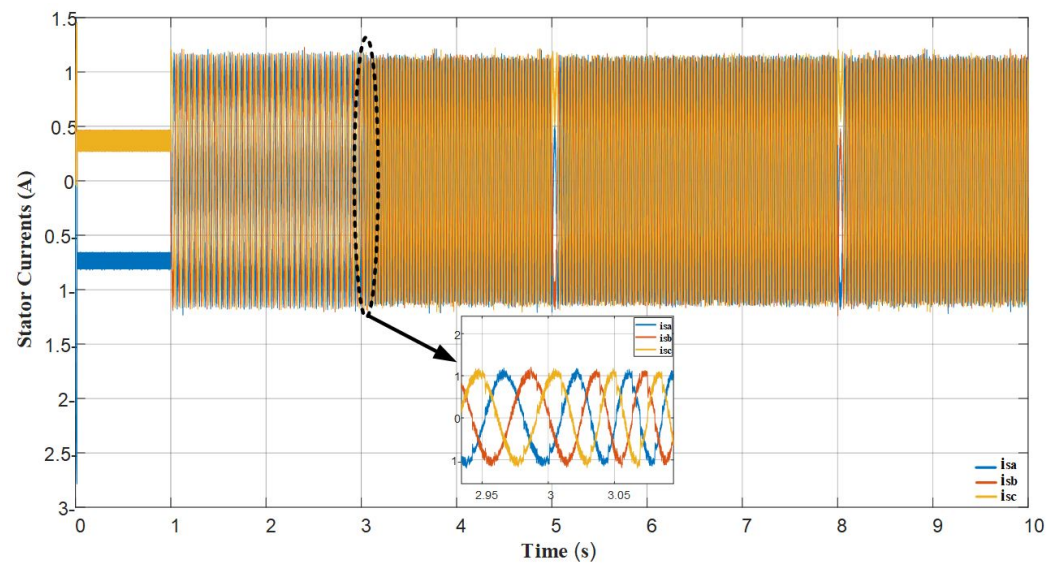


Figure 14. Three-phase currents for the conventional and improved strategies.

Figures 15–18 show the operation of the proposed 18-SS strategy at nominal speed for positive and negative rotations. Nominal torque (± 1.76 N.m) and rotor flux (0.945 Wb) were requested. The motor produced the nominal currents that are sinusoidal without any shock. It is noted that the torque and flux are well controlled around the nominal reference values in the positive and negative directions. The torque dynamic is fast since it lasted 0.65 ms.

Figure 19 shows the torque response in both the classical and the improved strategy when working at a high speed equal to the nominal speed. It is proven that the torque response in the improved strategy is superior to the torque response in the classical strategy in terms of torque ripple amplitude. The ripple amplitude in the classical strategy increased to a value 0.75 N.m due to the wrong effect of many VVs, according to what was proven in the above analytical study. However, the amplitude of the ripples in the torque response of the proposed strategy is 0.55 N.m.

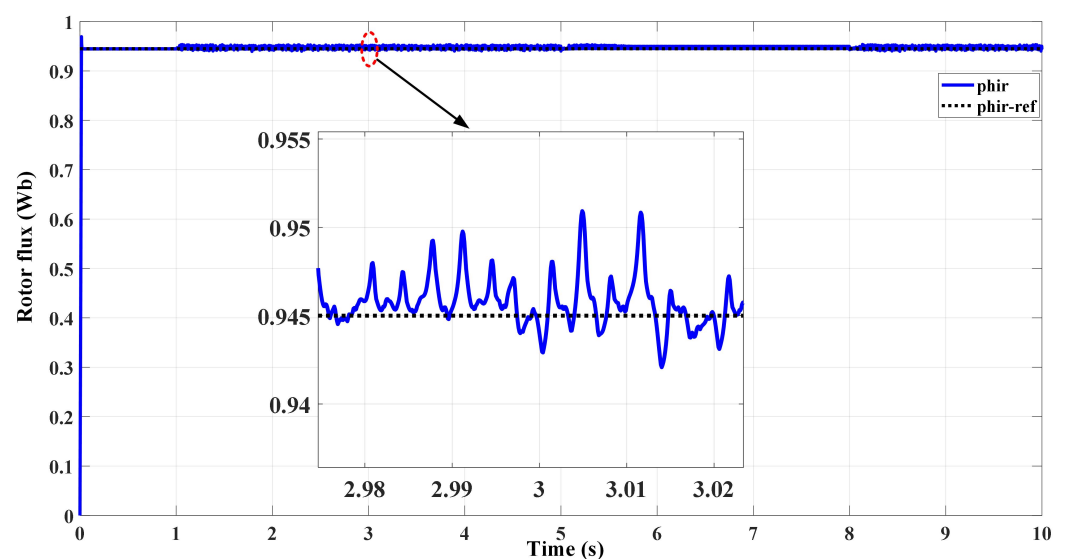


Figure 15. Rotor flux response of the proposed strategy for nominal speed.

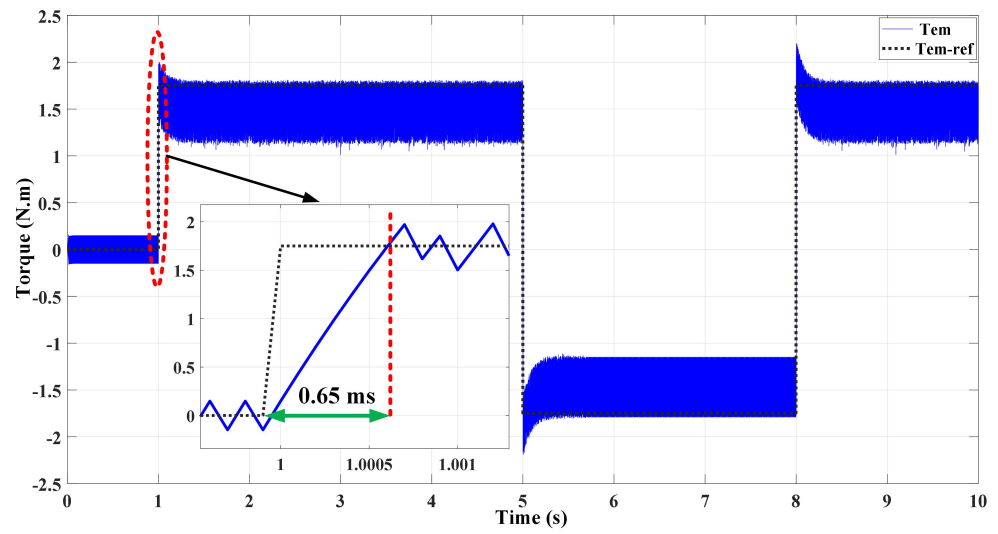


Figure 16. Torque response of the proposed strategy for nominal speed.

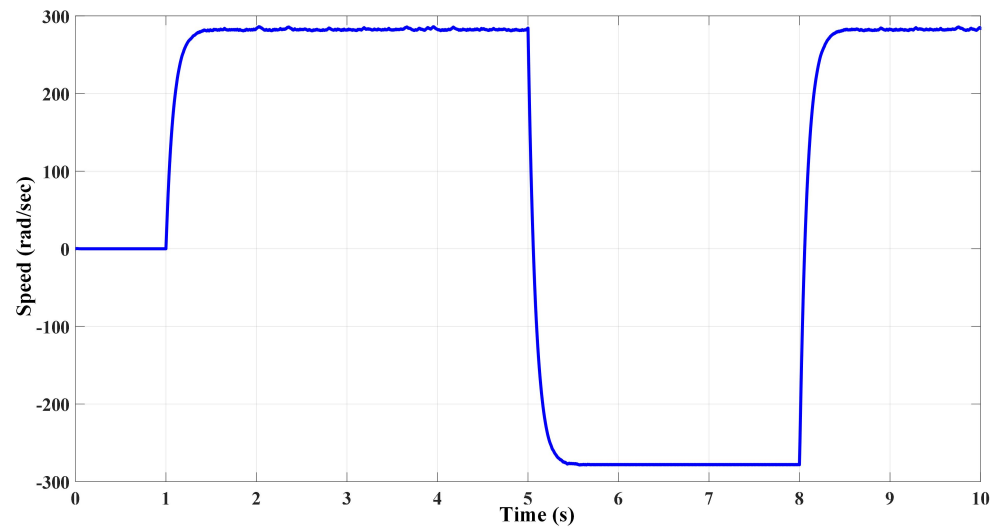


Figure 17. Speed response of the proposed strategy for nominal rotation.

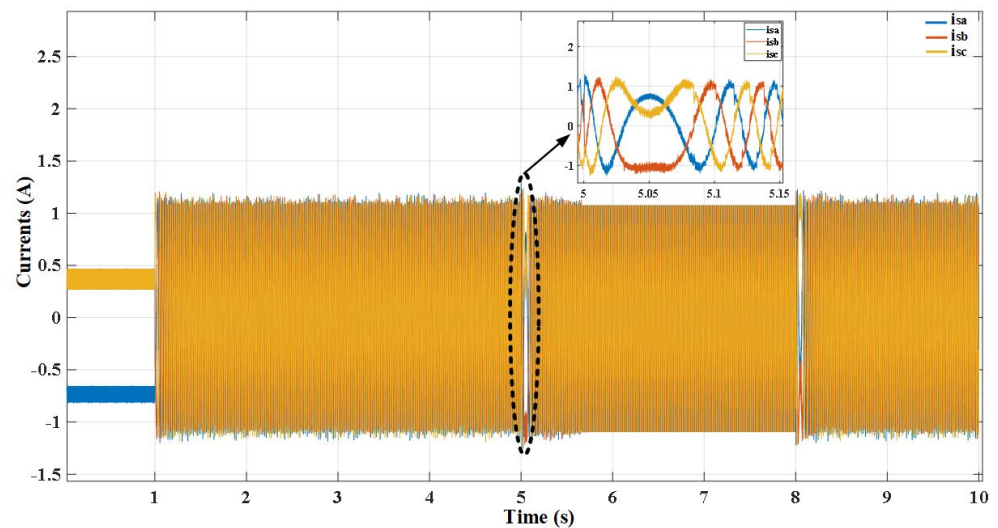


Figure 18. Motor currents of the proposed strategy for nominal speed.

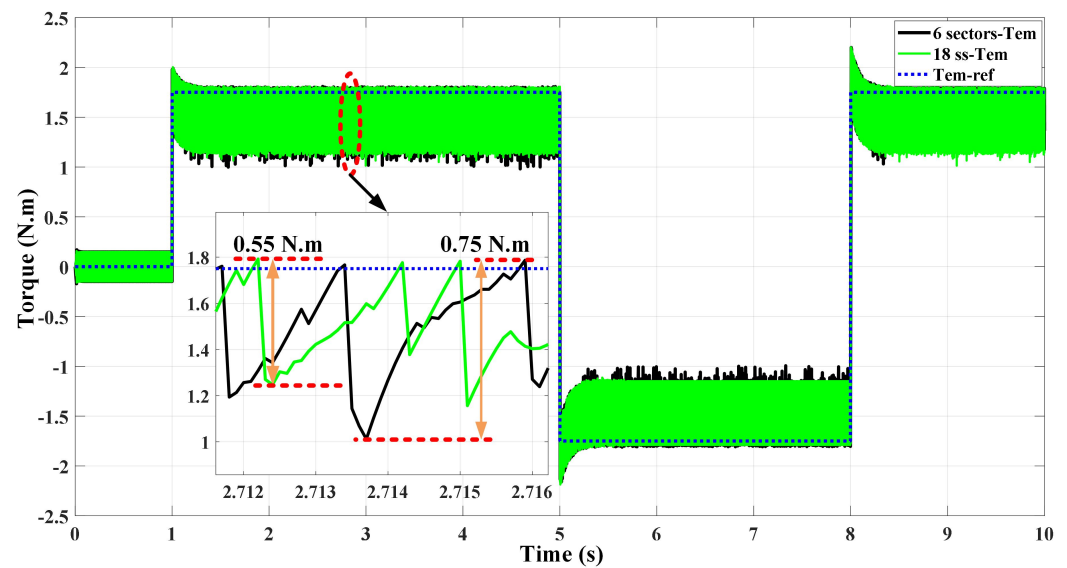


Figure 19. The torque response of both the classical and improved strategies at high speed is equal to the nominal speed.

Figure 20 shows the torque signal at nominal speed in both the conventional strategy and the improved strategy when the stator resistance is increased by 30%. It is clear that the improved strategy is robust with the change in resistance compared to the conventional strategy. This is due to the correct selection of the voltage vectors as a result of the analytical study. The traditional strategy suffered from increased torque ripples, rising to the value of 0.8 N.m, while it was 0.55 N.m in the improved strategy.

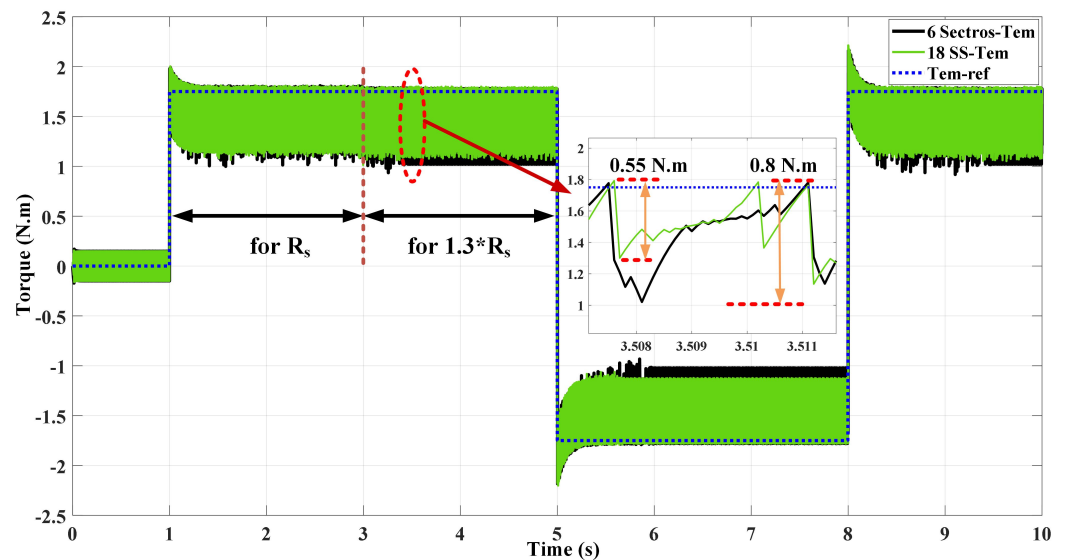


Figure 20. The torque signal of both the classical and improved strategies with R_s variation.

Figure 21 shows the six sectors and the eighteen sub-sectors of the two strategies which ensure that the two algorithms are working in parallel and both are ready to deliver the pulses to the inverter according to any required speed range.

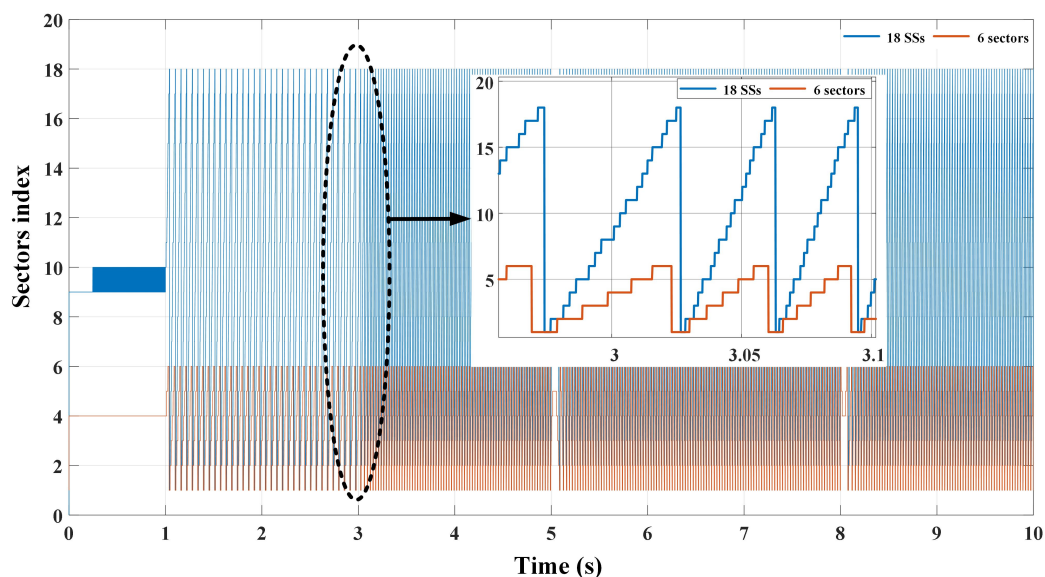


Figure 21. Sectors and sub-sectors of the conventional and improved strategy respectively.

To show the performance using the proposed (18) SS strategy at high speeds, especially its role in canceling the UCAs, two stages of the test were completed. First, the conventional (six)-sector DTRFC operated for a specific high speed ($0.75\% \omega_n$) and the UCAs were identified within the torque response. In the second stage, the conventional strategy was replaced with the proposed one which operated at the same high speed value, and investigated whether UCAs appeared. Based on the aforementioned two stages, an important comparison between the two torque signals of the (6-sector DTRFC) conventional strategy and the (18-SS DTRFC) proposed strategy was performed in Figures 22 and 23, respectively. The torque response in Figure 22, is plotted in the first sector with the applied VVs during the operation of the conventional (six sector) DTRFC strategy at high speed which is equal to ($\omega = 0.75 \times \omega_n$). The UCAs were indicated within small circles. It is noted that this strategy suffered from the presence of incorrectly switching states periodically in each sector. This is consistent with the results of the analytical study presented in Figure 3.

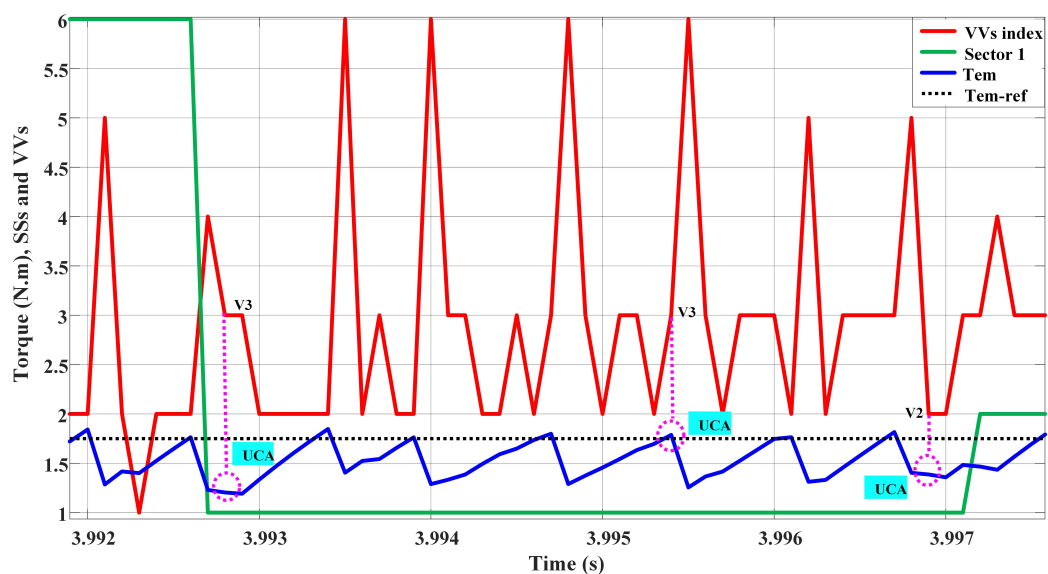


Figure 22. Torque response and applied voltage vectors of (6-sector) DTRFC strategy at high speed.

Figure 23 shows the torque response with the applied VVs during the first three SSs at the same high speed value ($0.75\% \omega_n$). It can be noted that the UCAs completely

disappeared in this strategy. This agrees with the results of the analytical study presented in Figure 23.

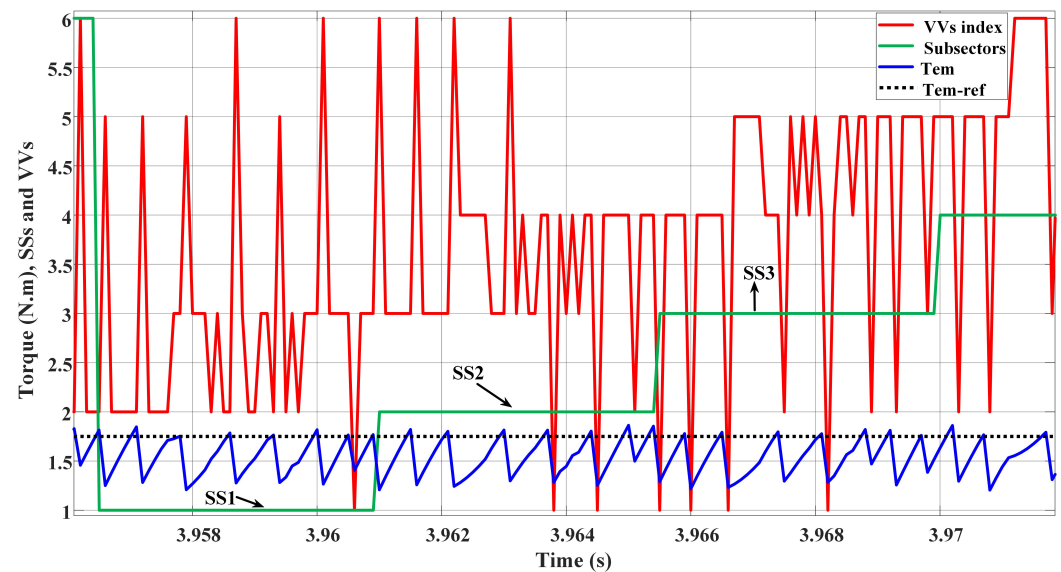


Figure 23. Torque response and applied voltage vectors of (18 SS) DTRFC strategy at high speed.

It is necessary to plot the switching frequency variations of inverter power transistors over the entire speed range since, unlike the FOC algorithm, the DTRFC algorithm operates with variable switching frequency. Figure 24 shows the switching frequency variations for the three strategies, 6-sector DTRFC, 18-SS DTRFC, and the combined algorithm, from zero speed to the nominal speed.

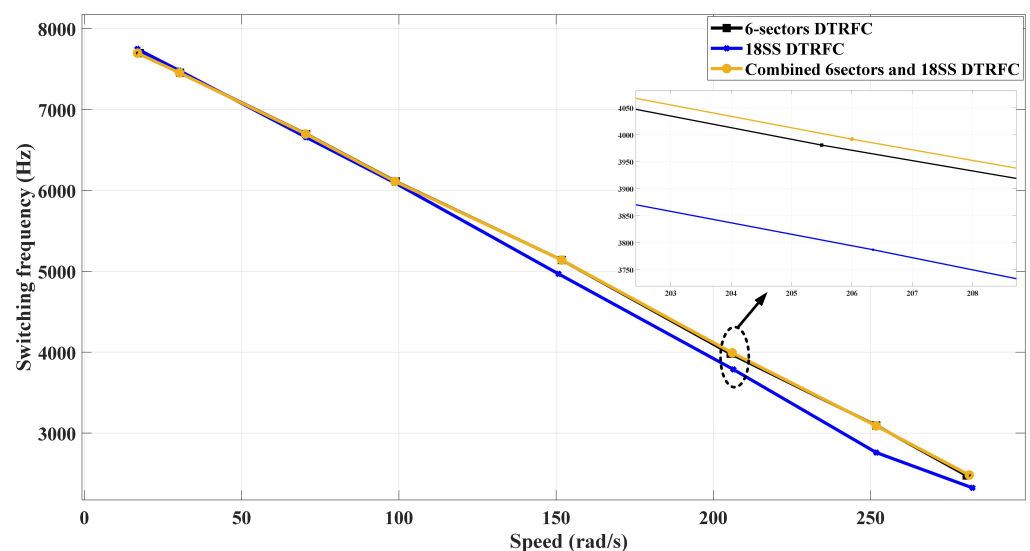


Figure 24. The switching frequency of the conventional and proposed strategies over the speed range.

It is noticed that the switching frequency values are high at low rotational speeds. This is due to the fact that the effective VV causes a severe change in the torque response because its amplitude is much greater than the back electromotive force (EMF) related to the speed. This results in an increase in the number of oscillations in the torque signal, which necessarily leads to an increase in the frequency switching. At high speeds, the application of the effective VV causes a slow change in the torque signal because its amplitude is close to the reverse electromotive force. Therefore, the number of oscillations is small, which causes a decrease in the value of the switching frequency. The value of the switching

frequency is the same for all above strategies within the low speed range. It is in the range (6–7.6 kHz) for the speed range (0:100 rad/s). As the speed increases, there is a slight difference in the switching frequency value of the three strategies and a lower value for the (18-SS DTRFC) strategy. For the speed value (206 rad/s), the switching frequency of the 18-SS DTRFC is 3.8 kHz, while in the conventional and combined strategies, it is approximately 4 kHz.

Table 4 provides a complete comparison of the performance of the upgraded 18-SS DTRFC vs. the conventional 6-sector DTRFC. It is evident from the comparison that the proposed technique performs superior to the conventional strategy at medium and high speeds. The suggested methodology reduces the ripple amplitude of the torque compared to the standard strategy. In addition, the switching frequency of the suggested method is less than that of the conventional technique at nominal speed. Furthermore, the enhanced technique is more resilient to changing motor parameters than the conventional strategy. The most crucial aspect of the improved method is that the switching table was constructed analytically, whereas the classical technique relies on the designer’s knowledge. Thus, the UCAs were eliminated from the enhanced approach, whereas the effect of these angles remains in the classic strategy. Except for the calculation of the sectors and the updated LUT, the computation time of the enhanced strategy is not significantly larger than that of the conventional one, as all the blocks are identical to those of the conventional one.

Table 4. Comprehensive comparison of the proposed approach to the conventional method.

Operating Parameters Values	Classical 6-Sector DTRFC	Improved 18-SS DTRFC
Torque ripples (low and medium speed)	0.55 N.m	0.55 N.m
Torque ripples (High speed)	0.75 N.m	0.55 N.m
Flux ripples	0.01 Wb	0.013 Wb
Switching frequency (low and medium speed)	6 to 7.8 kHz	6 to 7.8 kHz
Switching frequency (nominal speed)	3 kHz	2.5 kHz
Parameters variations	Weak	Strong
Lookup table construction	Designer’s knowledge	Analytically
UCAs	Exist	Fully eliminated
Computational time	18.5 μ s	22.3 μ s

10. Hardware Experimental Results

For the experimental verification of the proposed method, a test platform is prepared in the laboratory as illustrated in Figure 25, which includes a dSPACE card of the DS1103 family supported with ControlDesk monitoring GUI. In the setup, a squirrel cage three-phase induction motor 0.25 kW, 230/400 V, 50 Hz is used. The whole motor parameters of the tested IM are illustrated in Appendix B. The motor was fed from a 22.8 KVA three-phase Semikron inverter. The dc-link voltage was set at $E = 550$ V. The currents and the rotating speed of the IM are measured using hall-type LEM sensors and an 1024-pulse-per-revolution incremental encoder, respectively. All the measured electrical signals are filtered using separate first-order filters and then converted into digital signals using A/D channels within dSPACE. It is worth mentioning that the phase-voltage sensors are eliminated to increase the system reliability and decrease the total cost of the IM drive. The two components of the voltage vector VV were estimated by measuring the voltage of the dc-link, E , and the pulses of the inverter. A desktop computer is used to edit the control program and command the drive on the test rig. The experimental results of the conventional DTRFC strategy at a high speed ($\omega = 0.75 \times \omega_n$) and sampling time $T_s = 50$ (μ s) were carried out, as shown in Figure 26. The torque reference value is step-changed at the moments ($t = 0.9$ s) and ($t = 2.1$ s), respectively, from nominal reference torque (1.76 N.m) to the half nominal reference torque (0.88 N.m) and vice versa. It can be observed that the torque is well controlled around the reference values with high dynamics.

In Figure 27, the rotor flux Φ_r is shown, which is also well controlled around its reference nominal value ($\Phi_{r_ref} = 0.945$ Wb). The two-phase currents $i_{s\alpha}, i_{s\beta}$ are well regulated and have a response similar to the rotor flux and torque responses, respectively. The three-phase currents are sinusoidal currents with low distortion.

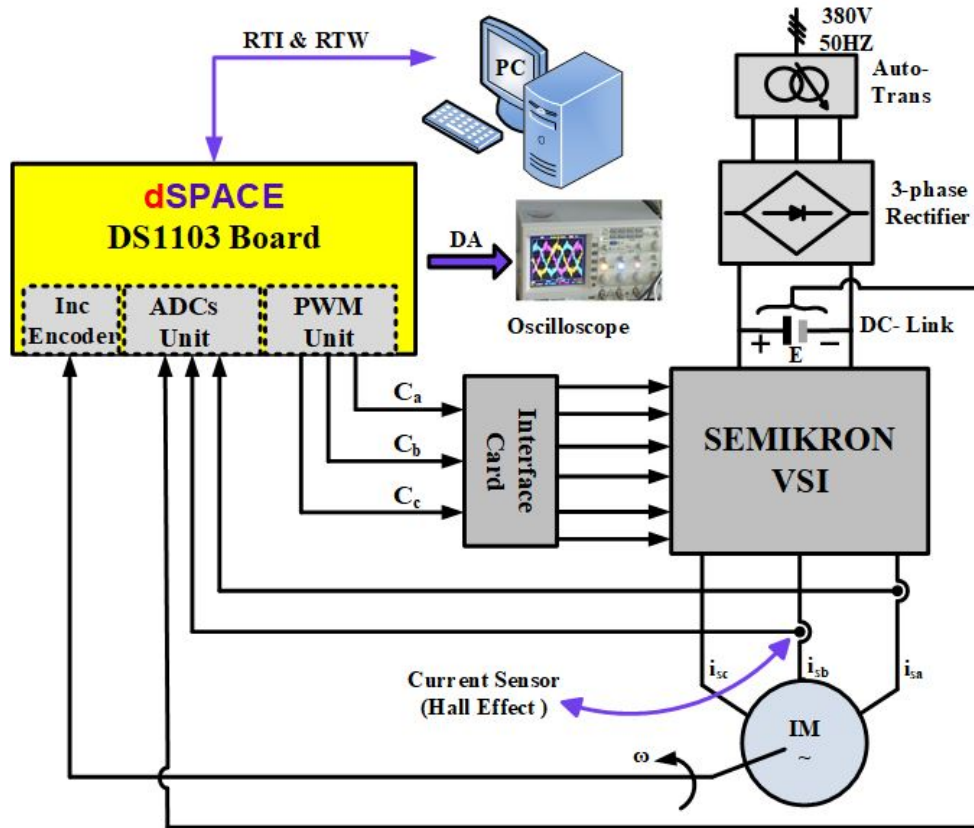


Figure 25. Experimental setup of IM-based drive system.

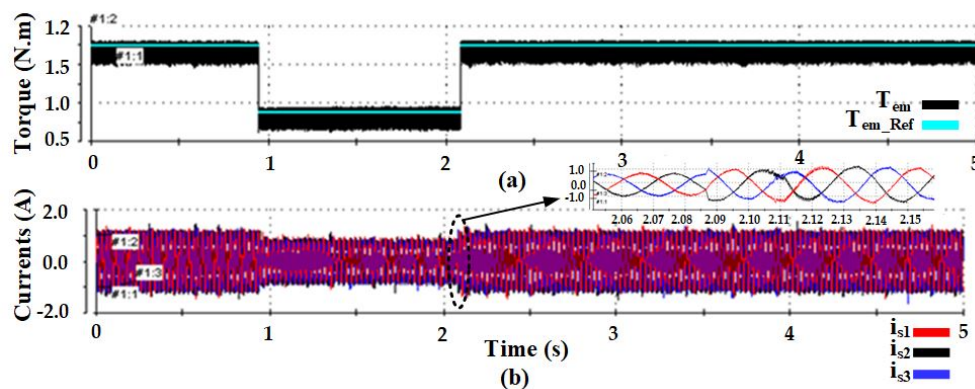


Figure 26. Experimental results of 6-sector DTRFC strategy: (a) torque response; and (b) three-phase currents.

The responses of the stator and rotor fluxes components ($\Phi_{s\alpha}, \Phi_{s\beta}, \Phi_{r\alpha}, \Phi_{r\beta}$) for the conventional 6-sector DTRFC, in synchronous reference frame, were estimated as shown in Figure 27. It is noted that the response of $\Phi_{s\alpha}$ is similar to the response of $\Phi_{r\alpha}$ in the steady state, while the response of component $\Phi_{s\beta}$ is similar to the responses of T_{em} and $i_{s\beta}$ in transient and steady states. The value of $\Phi_{r\beta}$ is equal to zero due to the orientation of the rotor flux vector along the α axis [42].

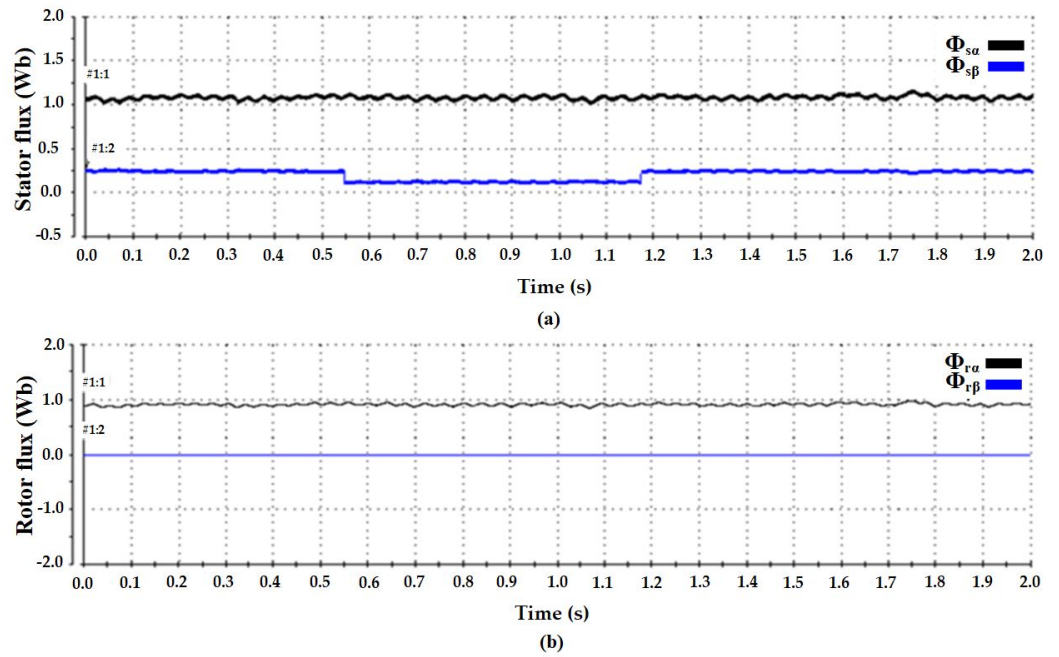


Figure 27. Flux at high speed ($75\% \omega_n$): (a) Stator flux components, (b) Rotor flux components.

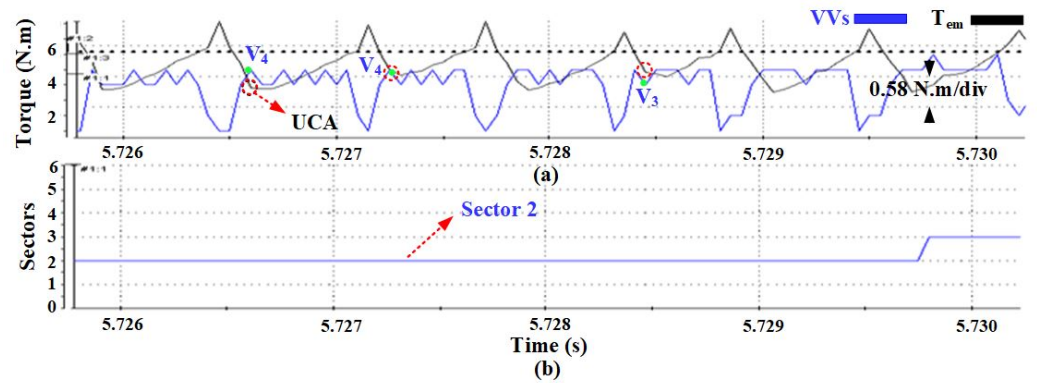


Figure 28. (a) Torque response towards VVs and (b) sector 2.

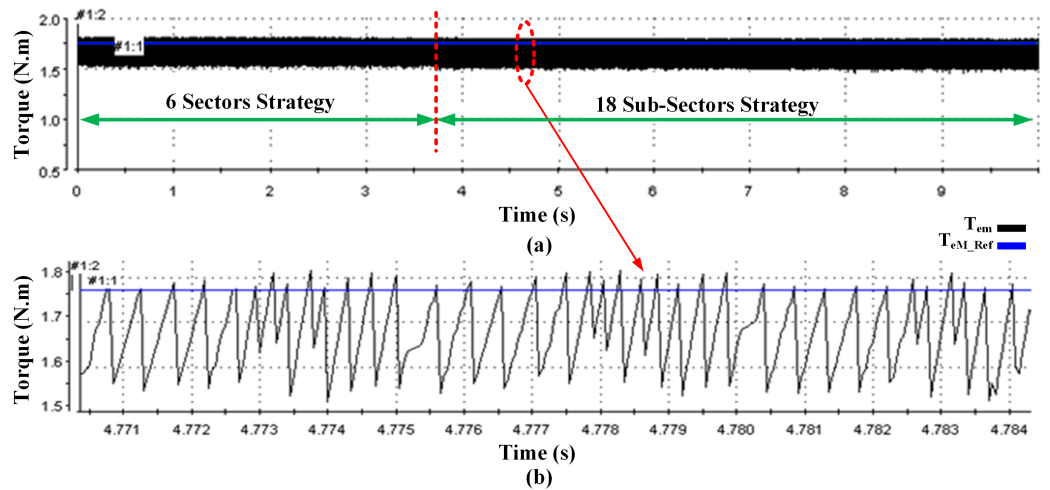


Figure 29. (a) Torque response towards VVs for the two strategies and (b) zoomed torque for 18-SS strategy.

The torque signal of the conventional 6-sector DTRFC strategy is plotted and zoomed in Figure 28 at high speed ($75\% \omega_n$) with the applied VVs in the second sector of the rotor flux vector path. The uncontrollable angles are outlined in small circles resulting from the two vectors, V_3 or V_4 . These two vectors are expected to increase the torque in the second sector as shown in Table 1. However, they decrease the torque in certain moments, i.e., there are UCAs. In Figure 29, the torque is well regulated around the reference value over the entire operation range using the combined strategy. It can be observed that the transition between the two strategies took place at (3.81 s), which is almost smoothly and quietly without any shock. The torque signal was zoomed in within the working range of the improved strategy, and it was found that the torque signal had no UCAs. The control decision signal that enables the transition between the two strategies is shown in Figure 30. The conventional strategy is allowed to deliver the pulses to the inverter when the value of the control decision signal is zero, while the proposed strategy is allowed to deliver the pulses to the inverter when the value of the control decision signal becomes one. The three-phase currents are sinusoidal without any shock at the transition moment. In Figure 31, the rotor flux is well regulated around the reference value (0.945 Wb). In a synchronous reference frame, the two phase stator currents $i_{s\alpha}$ and $i_{s\beta}$ have the same form as the rotor flux and torque, respectively. In Figure 32, the six sectors and the eighteen sub-sectors of both strategies are drawn in the same figure. Indeed, the two strategies are working in parallel and both are ready to deliver pulses to the inverter at any moment. In Figure 33, a transition speed value that allows the transition between two strategies is set as ($\omega T = 0.63 \times \omega_n$), which is equal to (180 rad/s). The conventional six-sector DTRFC is allowed to work when the motor speed is less than the aforementioned speed value, while the proposed 18SSs DTRFC strategy is allowed to work when the motor speed exceeds the above value.

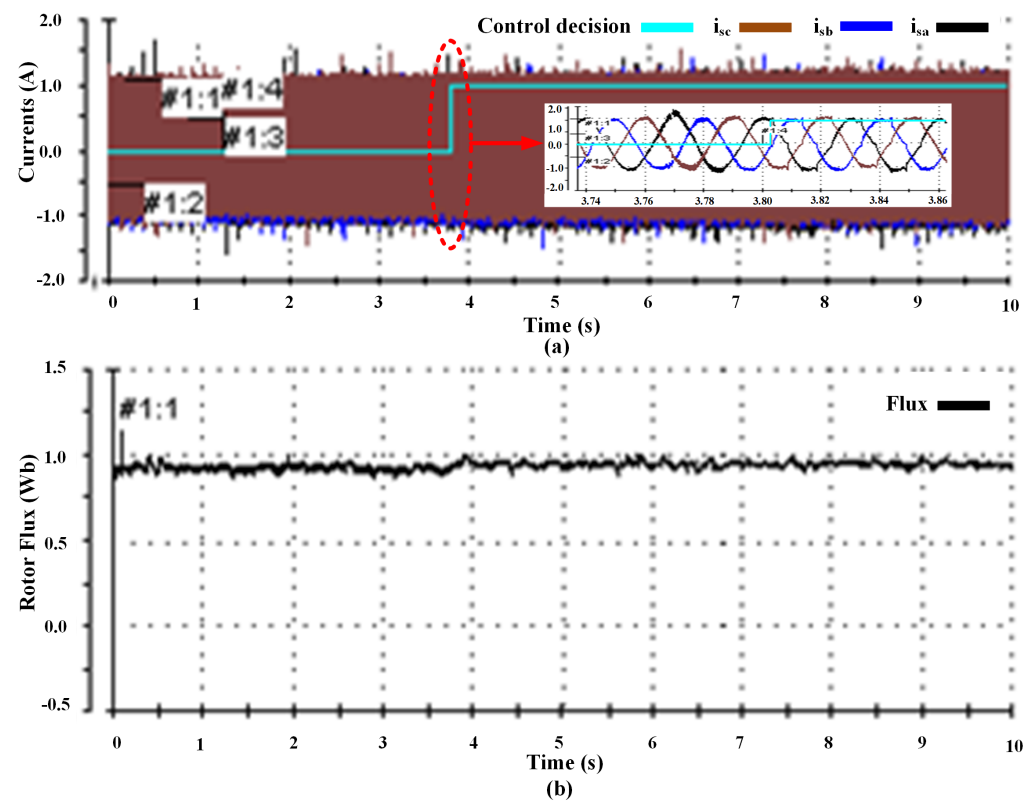


Figure 30. Experimental results of the two strategies: (a): stator currents; (b): rotor flux response.

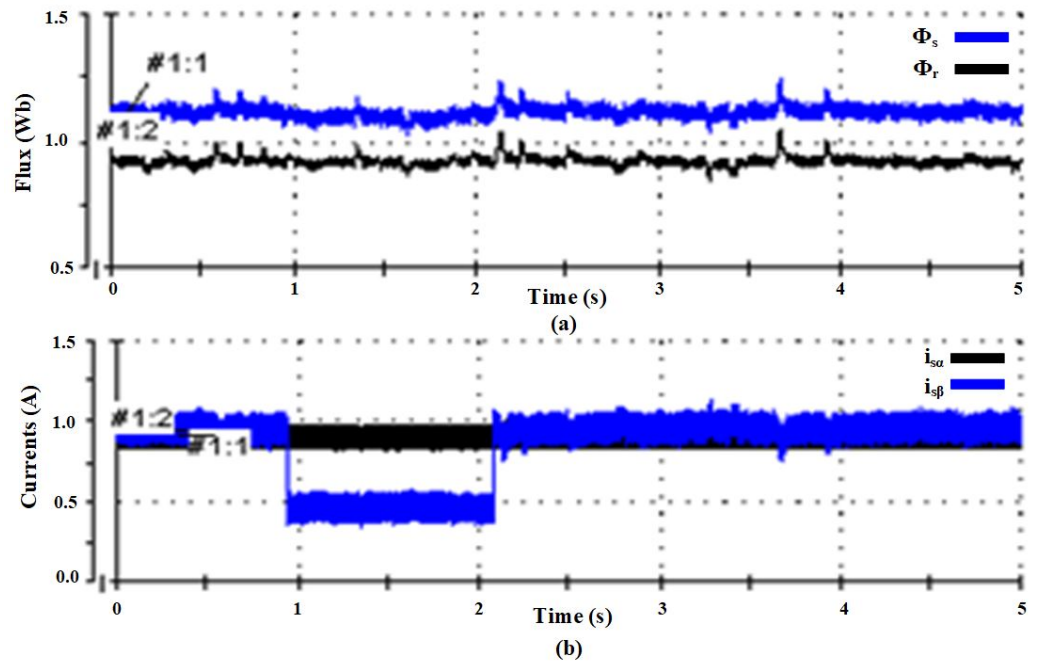


Figure 31. The components in synchronous reference frame: (a) stator and rotor fluxes responses; (b) stator currents responses.

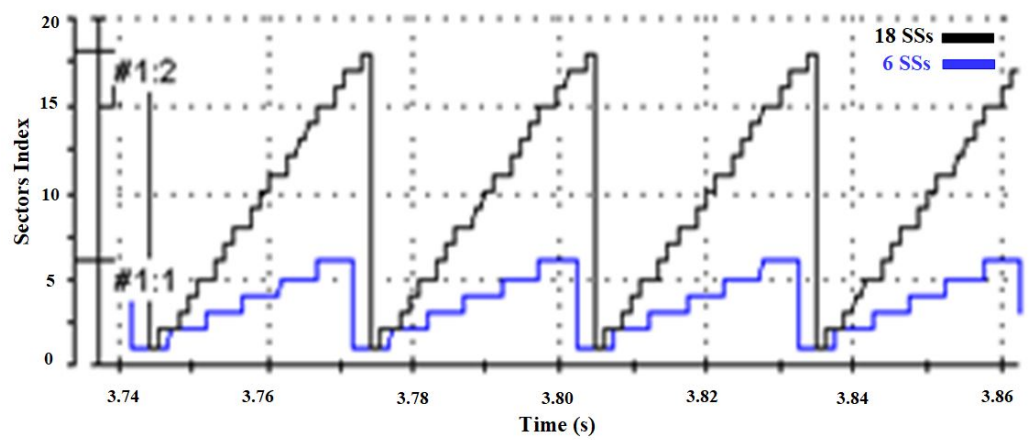


Figure 32. Sector index for the conventional 6 sectors and the proposed 18 SSs.

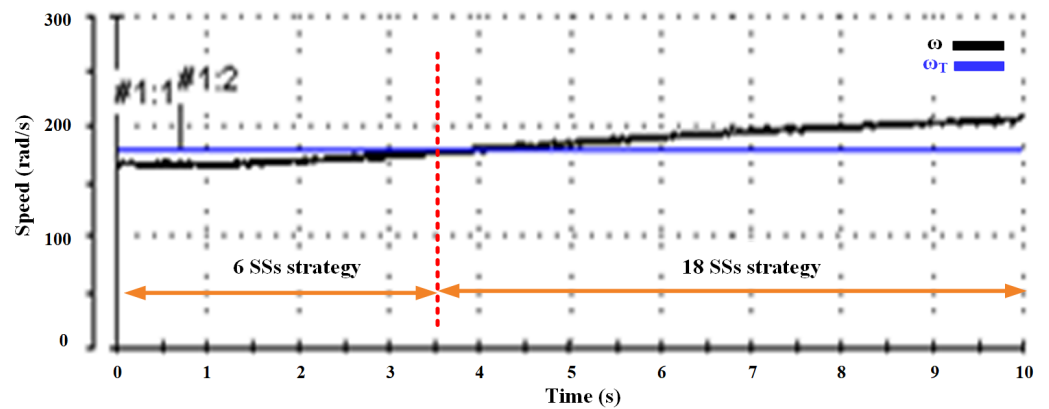


Figure 33. The DTRFC speed response with conventional 6 sectors and the proposed 18 SSs.

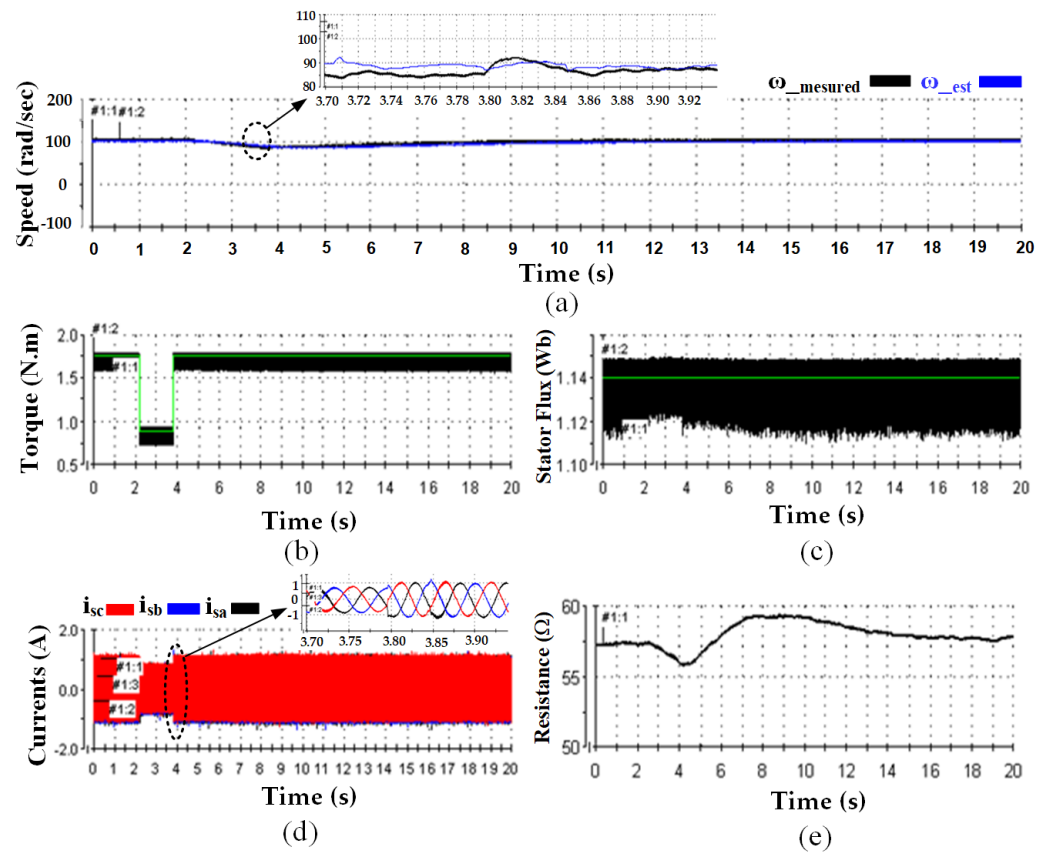


Figure 34. The DTC strategy with the adaptive estimator: (a) Speed response, (b) Torque response, (c) Stator flux, (d) Stator currents, (e) Stator resistance.

It is worth mentioning that, due to the poor performance of the traditional integrator, an adaptive Luenberger estimator was used in all previous experiments. In such an estimator, both the stator resistance as well as the speed were estimated using the two adaptive equations as in (18) and (19).

$$\omega_{est} = \left(K_{p\omega} + \frac{K_{I\omega}}{s} \right) \zeta_1; \zeta_1 = \hat{\Phi}_{s\beta} (i_{s\alpha}^s - \hat{i}_{s\alpha}^s) - \hat{\Phi}_{s\alpha} (i_{s\beta}^s - \hat{i}_{s\beta}^s) \quad (18)$$

$$R_{S_est} = \left(K_{pR} + \frac{K_{IR}}{s} \right) \zeta_2; \zeta_2 = i_{s\alpha}^s (i_{s\alpha}^s - \hat{i}_{s\alpha}^s) - i_{s\beta}^s (i_{s\beta}^s - \hat{i}_{s\beta}^s) \quad (19)$$

where, K_{ω} and K_R are the adaptation mechanisms of the speed and stator resistance estimation, respectively.

Figure 34 shows the results of testing the direct torque control strategy with the adaptive estimator at a speed equivalent to $\omega = 100$ rad/s. At the moment ($t = 2$ s), a reference torque step of (0.88 N.m) was made until the moment ($t = 4$ s) that the nominal reference value was requested again. The regulation state remained satisfied for both magnetic flux and electromagnetic torque with high dynamics. It is observed that the estimated speed ω_{est} followed well the measured speed $\omega_{measured}$ with a small error between them that did not exceed $\omega_{error} = 2\%$. The changes in the stator resistance was monitored during operation. Its value was approximately $R_{S_est} = 57 \Omega$, which was considered increased compared to the nominal resistance value. This expected increase in the resistance value is explained by the fact that the cooling at low speeds is at low levels in the motor, which leads to a rise in the temperature of the coils. The adaptation mechanisms of the speed constants of ($PI_{\omega} = 10$ and 100) were chosen. The values were chosen, taking into account the achievement of a rapid response to the estimated speed in the tracking of the measured speed with the lowest possible chattering in the steady state. With regard

to the stator resistance estimation, the adaptation constants of ($PI_R = 100$ and 100) were tuned.

Moreover, in Figure 34d, the motor currents are three-phase currents with a maximum value of 1.1 A for the electromagnetic torque's nominal value. With a change in torque from its nominal value to half of its nominal value, the maximum value of the current decreases to 0.9 A. With the recovery of the torque rise to its nominal value, the currents return to their nominal value. The influence of resistance change on currents is limited. The current signals are distorted due to the presence of hysteresis regulators inside the drive system.

Table 5 shows an experimentally comparison of the switching frequency between the improved strategy and the classical strategy when tested for a wide speed range. It is noted that the switching frequency has close values between the two strategies for a speed not exceeding 100 rad/s. When increasing the speed, it is noticed that the frequency of switching in the improved strategy decreases compared to the classical strategy. This is one of the advantages obtained from the improved strategy. The results of this table confirm the validity of the results of the analysis presented in Figure 24.

Table 5. Switching frequency comparison of classical and proposed DTRFC.

Speed Range (rad /s)	Classical DTC	Proposed DTC
100	6100 Hz	6000 Hz
150	5350 Hz	5100 Hz
200	4215 Hz	3900 Hz
250	3250 Hz	2850 Hz

11. Conclusions

This paper provided an analytical investigation of the DTRFC algorithm over the entire speed range in terms of UCAs. The proposed scheme with (18) SSSs was designed to eliminate the UCAs of certain VVs at medium and high speeds, which yields a correct torque response. The transition speed value at which the UCAs begin to appear has been precisely analytically determined. Furthermore, the proposed method combines the advantages of conventional and proposed strategies to work over a wide speed range. The experimental results have validated the feasibility and effectiveness of the proposed scheme in IM which drives over a wide speed range. The contributions of the proposed scheme were successfully achieved and summarised as follows:

- The use of a normal 6-sector DTRFC technique allows for simplicity at low speeds.
- High performance at medium and high speeds is due to the elimination of the uncontrollable angles of the torque response.
- Accurate analytical determination of the transition speed between traditional and improved strategy.
- The switching table is based on the analysis's findings, not on designer experience.
- There is no increase in the switching frequency due to the increased number of sectors.
- Robustness to the parameters variations.
- Lower chattering of the torque at high speed when compared with classical strategy.

Future work will include several important points, including the improvement of the performance of the control decision, so that it is an intelligent decision based on neural networks. This will be in addition to an improvement to the switching tables, such that the error and change of error are utilised for both the rotor flux and torque. Finally, taking into account the increase in the number of hysteresis regulator levels, it is necessary to invest in zero voltage vectors.

Author Contributions: Conceptualisation, M.M.A. and M.M.E.; methodology, M.M.A., M.M.E., I.M.A. and F.A.; software, M.M.A.; validation, M.M.A., M.M.E., I.M.A. and F.A.; formal analysis, M.M.A. and M.M.E.; investigation, M.M.A., M.M.E. and I.M.A.; resources, M.M.A. and M.M.E.; data curation, M.M.A.; writing—original draft preparation, M.M.A. and M.M.E.; writing—review and

editing, M.M.A., M.M.E., I.M.A. and F.A.; visualisation, M.M.A.; supervision, M.M.A., M.M.E., I.M.A. and F.A.; project administration, M.M.A., M.M.E., I.M.A. and F.A.; funding acquisition, M.M.A., M.M.E., I.M.A. and F.A. All authors have read and agreed to the published version of the manuscript.

Funding: This research received no external funding.

Institutional Review Board Statement: Not applicable.

Informed Consent Statement: Not applicable.

Data Availability Statement: Not applicable.

Conflicts of Interest: The authors declare no conflict of interest.

Appendix A

Table A1. Abbreviations.

Abbreviation	Definition
PWM	Pulse Width Modulation
FOC	Field-Oriented Control
DTC	Direct Torque Control
DTRFC	Direct Torque and Rotor Flux Control
UCAs	Uncontrollable angles
IM	Induction Motor
PMSM	Permanent Magnet Synchronous Motor
CSFC	Constant Switching Frequency Controller
VVs	Voltage Vectors
VSI	Voltage Source Inverter
HCs	Hysteresis Controllers
LUT	Lookup Table
SS	Sub-Sector

Appendix B

Table A2. The IM nameplate data and parameters.

Variable	Unit Value
Nominal voltage	230 / 400 V
Phase resistance stator	$R_s = 45.83 \Omega$
Phase resistance rotor	$R_r = 31 \Omega$
Phase inductance stator	$L_s = 1.24 \text{ H}$
Phase inductance rotor	$L_r = 1.11 \text{ H}$
Mutual inductance	$L_m = 1.05 \text{ H}$
Inertia	$J = 0.006 \text{ kg}\cdot\text{m}^2$
Friction factor	$F = 0.001 \text{ N}\cdot\text{m}\cdot\text{s}/\text{rad}$
Number of poles pairs	$P = 2$
Nominal stator flux	$\Phi_s = 1.14 \text{ Wb}$
Nominal rotor flux	$\Phi_r = 0.945 \text{ Wb}$
Nominal power	$P_n = 0.25 \text{ kW}$
Nominal frequency	$F = 50 \text{ Hz}$
Nominal speed	$\omega_n = 282 \text{ rad/s}$
Nominal torque	$T_{em} = 1.76 \text{ N}\cdot\text{m}$

References

1. Takahashi M.; Noguchi T. A New Quick-Response and High-Efficiency Control Strategy of an Induction Motor. *IEEE Trans. Ind. Appl.* **1986**, *IA-22*, 820–827. <https://doi.org/10.1109/TIA.1986.4504799>.
2. Buja G.; Kazmierkowski M. Direct Torque Control of PWM Inverter Fed AC Motors—A Survey. *IEEE Trans. Ind. Electron.* **2004**, *51*, 744–757. <https://doi.org/10.1109/TIE.2004.831717>.
3. Lascu C.; Boldea I.; Blaabjerg F. Variable-Structure Direct Torque Control—A Class of Fast and Robust Controllers for Induction Machine Drives. *IEEE Trans. Ind. Electron.* **2004**, *51*, 785–792. <https://doi.org/10.1109/TIE.2004.831724>.

4. Idris N.; Yatim A. Direct Torque Control of Induction Machines With Constant Switching Frequency and Reduced Torque Ripple. *IEEE Trans. Ind. Electron.* **2004**, *51*, 758–767. <https://doi.org/10.1109/TIE.2004.831718>.
5. Toh, C.; Idris, N.; Yatim, A. Constant and High Switching Frequency Torque Controller for DTC Drives. *IEEE Power Electron. Lett.* **2005**, *31*, 76–80. <https://doi.org/10.1109/LPEL.2005.851316>.
6. Naassani, A.; Monmasson, E.; Louis, J. Synthesis of Direct Torque and Rotor Flux Control Algorithms by Means of Sliding-Mode Theory. *IEEE Trans. Ind. Electron.* **2005**, *52*, 785–799. <https://doi.org/10.1109/TIE.2005.847581>.
7. Abad, G.; Rodriguez, A.; Poza, J. Two-level VSC Based Predictive Direct Torque Control of The Double Fed Induction Machine With Reduced Torque and Flux Ripples at Low Constant Switching Frequency. *IEEE Trans. Power Electron.* **2005**, *23*, 1050–1061. <https://doi.org/10.1109/TPEL.2008.921160>.
8. Ryu, J.; Lee, K.; Lee, J. A Unified Flux and Torque Control Method for DTC- Based Induction-Motor Drives. *IEEE Trans. Power Electron.* **2006**, *21*, 234–242. <https://doi.org/10.1109/TPEL.2005.861176>.
9. Nikzad, M.; Asaei, B.; Ahmadi, S. Discrete Duty-Cycle-Control Method for Direct Torque Control of Induction Motor Drives With Model Predictive Solution. *IEEE Trans. on Power Electron.* **2018**, *33*, 2317–2329. <https://doi.org/10.1109/TPEL.2017.2690304>.
10. Meesala, R.; Thippiripati, V. An Improved Direct Torque Control of Three-Level Dual Inverter Fed Open-Ended Winding Induction Motor Drive Based on Modified Look-Up Table. *IEEE Trans. Power Electron.* **2020**, *35*, 3906–3917. <https://doi.org/10.1109/TPEL.2019.2937684>.
11. Alsofyani, I.; Bak, Y.; Lee, K. Fast Torque Control and Minimized Sector-Flux Droop for Constant Frequency Torque Controller Based DTC of Induction Machines. *IEEE Trans. Power Electron.* **2019**, *34*, 12141–12153. <https://doi.org/10.1109/TPEL.2019.2908631>.
12. Yang, G.; Yang, J.; Li, S.; Wang, Y.; Hussain, H.; Deng, R.; Yan, L. A Sequential Direct Torque Control Scheme for Seven-Phase Induction Machines Based on Virtual Voltage Vectors. *IEEE Trans. Ind. Appl.* **2021**, *57*, 3722–3734. <https://doi.org/10.1109/TIA.2021.3068932>.
13. Alsofyani, I.; Lee, K. Enhanced Performance of Constant Frequency Torque Controller-Based Direct Torque Control of Induction Machines with Increased Torque-Loop Bandwidth. *IEEE Trans. Ind. Electron.* **2020**, *67*, 10168–10179. <https://doi.org/10.1109/TIE.2019.2959477>.
14. Cirrincione, M.; Pucci, M.; Vitale, G. A New Direct Torque Control Strategy for the Minimization of Common-Mode Emissions. *IEEE Trans. Ind. Appl.* **2006**, *24*, 504–517. <https://doi.org/10.1109/TIA.2005.863907>.
15. Deng, W.; Li, H.; Rong, J. A Novel Direct Torque Control of Matrix Converter-Fed PMSM Drives Using Dynamic Sector Boundary for Common-Mode Voltage Minimization. *IEEE Trans. Ind. Electron.* **2021**, *68*, 70–80. <https://doi.org/10.1109/TIE.2019.2962408>.
16. Lascu, C.; Jafarzadeh, S.; Fadali, S. Direct Torque Control With Feedback Linearization for Induction Motor Drives. *IEEE Trans. Power Electron.* **2017**, *32*, 2072–2080. <https://doi.org/10.1109/TPEL.2016.2564943>.
17. Naik, N.; Singh, S. A Comparative Analytical Performance of F2DTC and PIDTC of Induction Motor Using DSPACE-1104. *IEEE Trans. Ind. Electron.* **2015**, *62*, 7350–7359. <https://doi.org/10.1109/TIE.2015.2463758>.
18. Alsofyani, I.; Idris, N. Simple flux regulation for improving state estimation at very low and zero speed of a speed sensorless direct torque control of an induction motor. *IEEE Trans. Power Electron.* **2015**, *2*, 3027–3035. <https://doi.org/10.1109/TPEL.2015.2447731>.
19. Alsofyani, I.; Idris, N.; Lee, K. Dynamic Hysteresis Torque Band for Improving the Performance of Lookup-Table-Based DTC of Induction Machines. *IEEE Trans. Power Electron.* **2018**, *33*, 7959–7970. <https://doi.org/10.1109/TPEL.2017.2773129>.
20. Wang, X.; Wang, Z.; Xu, Z.; Hu, Y. Optimization of Torque Tracking Performance for Direct-Torque-Controlled PMSM Drives With Composite Torque Regulator. *IEEE Trans. Ind. Electron.* **2020**, *67*, 10095–10108. <https://doi.org/10.1109/TIE.2019.2962451>.
21. Wang, M.; Sun, D.; Ke, W.; Nian, H. A Universal Lookup Table-Based Direct Torque Control for OW-PMSM Drives. *IEEE Trans. Power Electron.* **2021**, *36*, 6188–6191. <https://doi.org/10.1109/TPEL.2020.3037202>.
22. Wu, X.; Huang, W.; Lin, X.; Jiang, W.; Zhao, Y.; Zhu, S. Direct Torque Control for Induction Motors Based on Minimum Voltage Vector Error. *IEEE Trans. Ind. Electron.* **2021**, *68*, 3794–3804. <https://doi.org/10.1109/TIE.2020.2987283>.
23. Nasr, A.; Gu, C.; Wang, X.; Buticchi, G.; Bozhko, S.; Gerada, C. Torque-Performance Improvement for Direct Torque-Controlled PMSM Drives Based on Duty-Ratio Regulation. *IEEE Trans. Power Electron.* **2022**, *37*, 749–760. <https://doi.org/10.1109/TPEL.2021.3093344>.
24. Elgbaily, M.; Anayi, F.; Packianather, M. Genetic and particle swarm optimization algorithms based direct torque control for torque ripple attenuation of induction motor. *Mater. Today: Proc.* **2022**, *67*, 577–590. <https://doi.org/10.1016/j.matpr.2022.08.293>.
25. Fahassa, C.; Zahraoui, Y.; Akherraz, M.; Kharrich, M.; Elattar, E. Induction Motor DTC Performance Improvement by Inserting Fuzzy Logic Controllers and Twelve-Sector Neural Network Switching Table. *Mathematics* **2022**, *10*, 1357. <https://doi.org/10.3390/math10091357>.
26. Awwad, A.E. Dynamic Performance Enhancement of a Direct-Driven PMSG-Based Wind Turbine Using a 12-Sectors DTC. *World Electr. Veh. J.* **2022**, *13*, 123. <https://doi.org/10.3390/wevj13070123>.
27. El Haissouf, M.; El Haroussi, M.; Ba-Razzouk, A. DSP In the Loop implementation of an enhanced Direct Torque Control for Induction Motor drive. In Proceedings of the 2022 IEEE 2nd International Conference on Innovative Research in Applied Science, Engineering and Technology (IRASET), Meknes, Morocco, 3–4 March 2022; <https://doi.org/10.1109/IRASET52964.2022.9738073>.
28. Elgbaily, M.; Anayi, F.; Packianather, M. Performance Improvement Based Torque Ripple Minimization for Direct Torque Control Drive Fed Induction Motor Using Fuzzy Logic Control. In *Control, Instrumentation and Mechatronics: Theory and Practice*; Springer Nature: Singapore, 2022; pp. 416–428. https://doi.org/10.1007/978-981-19-3923-5_36.

29. Suresh, S.; Rajeevan, P.P. Virtual Space Vector Based Direct Torque Control Schemes for Induction Motor Drives. *IEEE Trans. Ind. Appl.* **2020**, *56*, 2719–2728. <https://doi.org/10.1109/TIA.2020.2978447>.
30. Wu, Z.; Zhou, J.; Zheng, G.; Li, T.; Zhu, Z. New Eighteen-sector Direct Torque Control Based on Duty Ratio Modulation. In Proceedings of the 2019 Journal of Physics 2nd International Symposium on Power Electronics and Control Engineering (ISPECE 2019), Tianjin, China, 22–24 November 2019; <https://doi.org/10.1088/1742-6596/1449/1/012033>.
31. Bhangale, S.V.; Kumar, R.; Bhangale, K. 18-Sector Direct Torque Controlled Strategy with Improved Stator Flux Estimator for Induction Motor Drive. In Proceedings of the 2018 IEEE 8th IEEE India International Conference on Power Electronics (IICPE), Jaipur, India, 13–15 December 2018; <https://doi.org/10.1109/IICPE.2018.8709571>.
32. Jibril, M. 24 sectors DTC control with fuzzy hysteresis comparators for DFIM fed by three-level inverter. *ScienceOpen Preprints* **2021**, *12*, 141–154. <https://doi.org/10.37394/232017.2021.12.19>
33. Kim, S.-K.; Kim, J.S.; Lee, Y.I. Model predictive control (MPC) based direct torque control (DTC) of permanent magnet synchronous motors (PMSMs). In Proceedings of the IEEE International Symposium on Industrial Electronics, Taipei, Taiwan, 28–31 May 2013. <https://doi.org/10.1109/ISIE.2013.6563637>.
34. Li, Y.-H.; Wu, T.-X.; Zhai, D.-W.; Zhao, C.-H.; Zhou, Y.-F.; Qin, Y.-G.; Su, J.-S.; Qin, H. Hybrid Decision Based on DNN and DTC for Model Predictive Torque Control of PMSM. *Symmetry* **2022**, *14*, 693. <https://doi.org/10.3390/sym14040693>.
35. Englert, T.; Grüner, S.; Graichen, K. Model predictive torque control of permanent magnet synchronous machines. *IFAC-PapersOnLine* **2017**, *50*, 758–763. <https://doi.org/10.1016/j.ifacol.2017.08.249>.
36. Aziz, A.G.M.A.; Rez, H.; Diab, A.A.Z. Robust Sensorless Model-Predictive Torque Flux Control for High-Performance Induction Motor Drives. *Mathematics* **2021**, *9*, 403. <https://doi.org/10.3390/math9040403>.
37. Kakouche, K.; Rekioua, T.; Mezani, S.; Oubelaid, A.; Rekioua, D.; Blazek, V.; Prokop, L.; Misak, S.; Bajaj, M.; Ghoneim, S.S.M. Model Predictive Direct Torque Control and Fuzzy Logic Energy Management for Multi Power Source Electric Vehicles. *Sensors* **2022**, *22*, 5669. <https://doi.org/10.3390/s22155669>.
38. Alshbib, M.M.; Elgbaily, M.M.; Anayi, F. An In-depth Analytical Study of the Switching States of Direct Torque Control Algorithm of an Induction Motor Over the Entire Speed Range. In Proceedings of the 1st International Electronic Conference on Machines and Applications (IECMA-2022), e-conference at <https://iecma2022.sciforum.net>, 15–30 September 2022; <https://doi.org/10.3390/IECMA2022-12900>.
39. Buja, G.; Menis, R. Steady-State Performance Degradation of a DTC IM Drive Under Parameter and Transduction Errors. *IEEE Trans. Ind. Electron.* **2008**, *55*, 1749–1760. <https://doi.org/10.1109/TIE.2008.917112>.
40. O'Rourke, C.J.; Qasim, M.M.; Overlin, M.R.; Kirtley, J.L. A Geometric Interpretation of Reference Frames and Transformations: Dq0, Clarke and Park. *IEEE Trans. Energy Convers.* **2019**, *34*, 2070–2083. <https://doi.org/10.1109/TEC.2019.2941175>.
41. Kabache, N.; Moulahoum, S.; Houassine, H. FPGA Implementation of direct Rotor Field Oriented Control for Induction Motor. In Proceedings of the 2013 IEEE 18th International Conference on Methods & Models in Automation & Robotics (MMAR), Miedzydroje, Poland, 26–29 August 2013; <https://doi.org/10.1109/MMAR.2013.6669958>.
42. Elgbaily, M.; Anayi, F.; Alshbib, M.M. A Combined Control Scheme of Direct Torque Control and Field-Oriented Control Algorithms for Three-Phase Induction Motor: Experimental Validation. *Mathematics* **2022**, *10*, 3842. <https://doi.org/10.3390/math10203842>.

Disclaimer/Publisher's Note: The statements, opinions and data contained in all publications are solely those of the individual author(s) and contributor(s) and not of MDPI and/or the editor(s). MDPI and/or the editor(s) disclaim responsibility for any injury to people or property resulting from any ideas, methods, instructions or products referred to in the content.